nature portfolio

https://doi.org/10.1038/s41586-026-10919-4

Supplementary information

Electronic-resonance enhanced molecule for perovskite solar cells

In the format provided by the authors and unedited

Supplementary Materials for

Electronic-resonance Enhanced Molecule for Perovskite Solar Cells

Xiaoxiao Wu[1,2†], Wenwen Kou[1,2†], Zewei Li[4], Tiankai Zhang[3]*, Guiying Xu[1,2], Busheng Zhang[4], Heyi Yang[5], Shengyu Li[1,2], Yunxiu Shen[1,2], Tingting Xu[1,2], Yeyong Wu[1,2], Yue Yin[1,2], Haiyang Chen[1,2], Qinrong Cheng[1,2,6], Xian-Kai Chen[4]*, Yaowen Li[1,2]*, and Yongfang Li[1,2,7]

[1] State Key Laboratory of Bioinspired Interfacial Materials Science, College of Chemistry, Chemical Engineering and Materials Science, Soochow University, Suzhou 215123, P. R. China

[2] Suzhou Key Laboratory of Novel Semiconductor-optoelectronics Materials and Devices, College of Chemistry, Chemical Engineering and Materials Science, Soochow University, Suzhou, 215123, Jiangsu, P. R. China

[3] School of Materials Science and Engineering, Southeast University, Nanjing, 211189, China

[4] Institute of Functional Nano & Soft Materials (FUNSOM), Soochow University, Suzhou, Jiangsu 215123, P.R. China

[5] Center of Advanced Optoelectronic Materials, College of Materials and Environmental Engineering, Hangzhou Dianzi University, Hangzhou 310018, China

[6] Suzhou Sunflex New Energy Company Limited, Suzhou 215100, China

[7] Beijing National Laboratory for Molecular Sciences; CAS Key Laboratory of Organic Solids, Institute of Chemistry, Chinese Academy of Sciences, Beijing 100190, P. R. China

*Corresponding author Email: tiankai.zhang@seu.edu.cn (T.K.Z.); xkchen@suda.edu.cn (X.K.C.); ywli@suda.edu.cn (Y.W.L.)

†These authors contributed equally to this work.

Table of Contents

Supplementary Notes

Supplementary Note 1. Material Synthesis

Synthesis of FTPA-CPA:

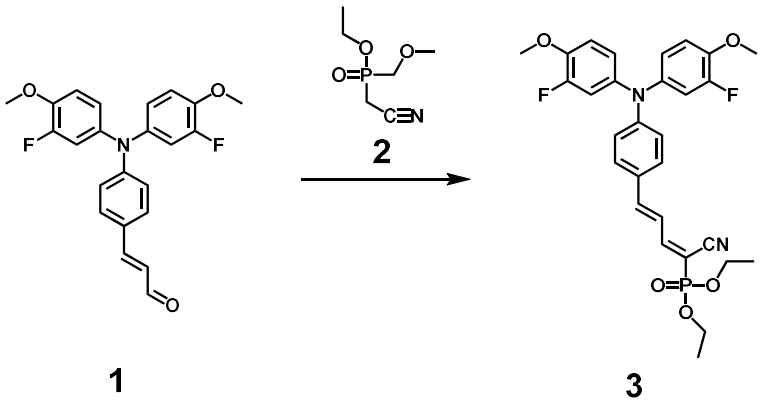

Compound **1** (5 g, 12.6 mmol) and compound **2** (6.7 g, 37.8 mmol) were added in a flask, then toluene (100 mL) with piperidine (1.5 mL) were used to dissolve them. Under an argon atmosphere, the mixture was stirred at 110 °C overnight. After reaction completion, the solvent was distilled off under reduced pressure. The residue was purified with column chromatography on silica gel using ethyl acetate as the eluent to give a red solid compound **3** (3.6 g, 52% yield).

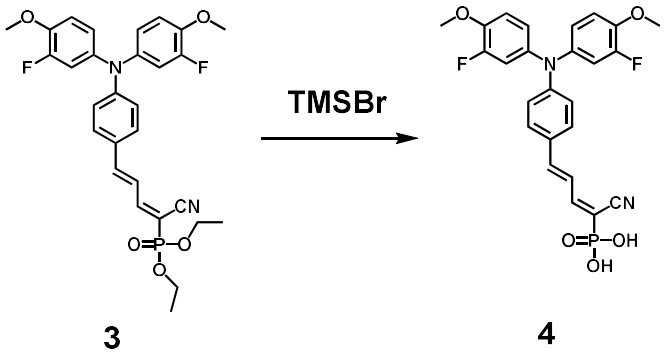

Compound **3** (3.6 g, 6.5 mmol) and TMSBr (16.8 g, 110 mmol) were added in a flask, then dichloromethane (125 mL) was us ed to dissolve them. Under an argon atmosphere, the mixture was stirred at room temperature overnight. After reaction, add 10 mL of methanol to quench the TMSBr. The solvent was distilled off under reduced pressure. The residue was added to petroleum ether to obtain the product as a yellow solid FTPA-CPA (Compound **4**) (2.5 g, 78% yield). ^{1}H NMR (400 MHz, DMSO-*d*6) δ 7.61 (dd, *J* = 17.0, 11.3 Hz, 1H), 7.51 (d, *J* = 8.8 Hz, 2H), 7.36 (d, *J* = 15.1 Hz, 1H), 7.18 (t, *J* = 9.3 Hz, 2H), 7.06 (dd, *J* = 12.6, 2.6 Hz, 2H), 7.01–6.93 (m, 3H), 6.80 (d, *J* = 8.9 Hz, 2H), 3.85 (s, 6H). ^{13}C NMR (101 MHz DMSO-d_6) δ 156.19, 156.13, 153.32, 150.87, 149.99, 146.25, 145.19, 145.08, 139.23, 139.14, 130.17, 127.47, 122.87, 122.84, 121.19, 121.02, 119.25, 116.82, 115.21, 115.18, 114.62, 114.43, 105.14, 103.24, 56.61. HR-MS (MALDI-TOF) m/z calcd. for ($C_{25}H_{21}F_2N_2O_5P$): 498.12. Found: 498.19.

Synthesis of FMTPA-CPA:

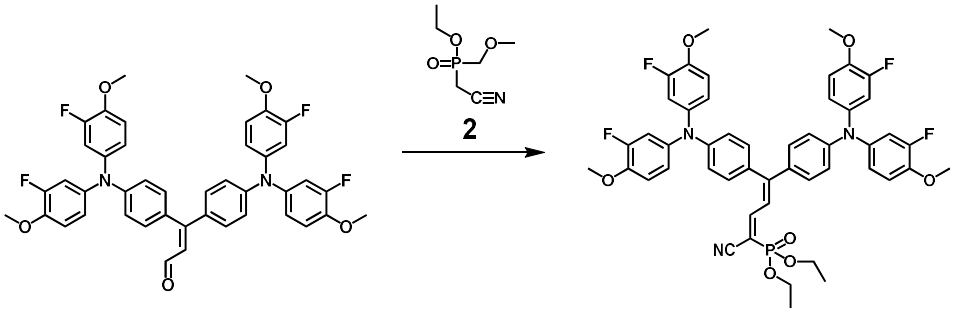

5 6

Compound **5** (5 g, 6.6 mmol) and compound **2** (3.5 g, 19.8 mmol) were added in a flask, then toluene (80 mL) with piperidine (1.2 mL) were used to dissolve them. Under an argon atmosphere, the mixture was stirred at 110 °C overnight. After reaction completion, the solvent was distilled off under reduced pressure. The residue was purified with column chromatography on silica gel using ethyl acetate as the eluent to give a dark red solid compound 6 (3.8 g, 63% yield).

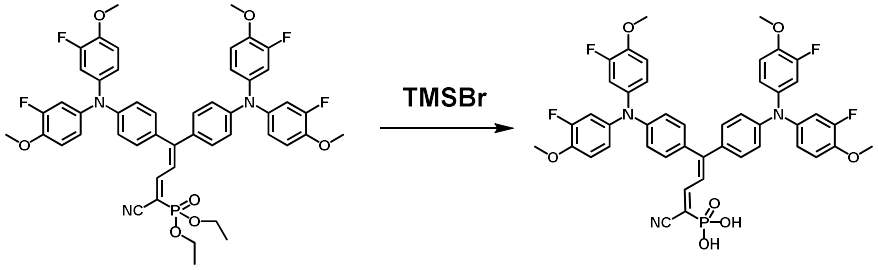

6 7

Compound **6** (3.8 g, 4.2 mmol) and TMSBr (10.7 g, 70 mmol) were added in a flask, then dichloromethane (80 mL) was used to dissolve them. Under an argon atmosphere, the mixture was stirred at room temperature overnight. After reaction, add 10 mL of methanol to quench the TMSBr. The solvent was distilled off under reduced pressure. The residue was added to petroleum ether to obtain the product as a yellow solid FMTPA-CPA (Compound **7**) (2.6 g, 73% yield). ^{1}H NMR (600 MHz, DMSO-*d*6) δ 8.37 (s, 1H), 7.38 (dd, J=16.9, 11.8 Hz, 1H), 7.20 (d, J=8.8 Hz, 2H), 7.14 (dt, J=9.3, 4.6 Hz, 4H), 7.06 (dd, J=12.5, 2.3 Hz, 2H), 7.04–6.98 (m, 4H), 6.96 (d, J=8.4 Hz, 2H), 6.92 (d, J=8.6 Hz, 2H), 6.85–6.82 (m, 1H), 6.80 (d, J=8.5 Hz, 2H), 6.77 (d, J=8.8 Hz, 2H), 3.81 (s, 12H). ^{13}C NMR (151 MHz, DMSO-d_6) δ 152.92, 151.26, 149.62, 148.81, 145.01, 144.94, 139.43, 139.33, 131.97, 130.33, 122.82, 122.70, 119.12, 118.68, 115.20, 114.56, 114.44, 114.32, 56.60, 51.86, 44.14. HR-MS (MALDI-TOF) m/z calcd. for ($C_{47}H_{40}F_4N_3O_7P$): 837.22. Found:837.32.

Supplementary Note 2. The discussion of molecular configuration

For free molecules, FTPA-CPA tends to exhibit E configuration while FMTPA-CPA tends to exhibit Z configuration. Here, we exploited the B3LYP-D3(BJ) to evaluate the intrinsic energies of both E and Z configurations of free molecules.[1,2,3] As shown in

Supplementary Fig. 9, the energy differences between E and Z configurations of FTPA-CPA and FMTPA-CPA are −0.046 eV and 0.071 eV, respectively, implying that FTPA-CPA tends to exhibit E configuration while FMTPA-CPA tends to exhibit Z configuration. Quantification of the ratio between E and Z configurations can be conducted using the energy differences results according to Boltzmann distribution equation.[4,5]

$$\boldsymbol{\rho(Z) = \frac{e^{-E_Z/(k_BT)}}{e^{-E_Z/(k_BT)} + e^{-E_E/(k_BT)}}}$$

$$\boldsymbol{\rho(E) = \frac{e^{-E_E/(k_BT)}}{e^{-E_Z/(k_BT)} + e^{-E_E/(k_BT)}}}$$

In this equation, $\rho(Z)$ and $\rho(E)$ are the probability of the Z and E configurations with the energies E_Z and E_E, respectively, and k_B is the Boltzmann constant. Consequently, FTPA-CPA exhibits 85% for E configuration and 15% for Z configuration, and FMTPA-CPA exhibits 8% for E configuration and 92% for Z configuration**.**

We employed ^{1}H NMR and ^{31}P NMR spectroscopy to determine molecular configuration.[6] Before conducting NMR measurement, we first analyzed the chemical environment of E and Z configuration by electrostatic surface potential (ESP) calculations. As shown in **Supplementary Fig. 15**, the H and P atoms adjacent to the C=C double bond that are assigned to the E configuration all exhibit lower electrostatic potential (i.e., higher electron density) compared to Z configuration in both FTPA-CPA and FMTPA-CPA. Therefore, E configuration in FTPA-CPA and FMTPA-CPA appears at lower chemical shift (δ) relative to the Z configuration.[7,8] In ^{1}H NMR measurement, FTPA-CPA powder with free molecule structure exhibits two distinct sets of signals in the vinylic proton (i position of FTPA-CPA in **Supplementary Fig. 1a**), at 7.57-7.64 ppm and 7.68-7.72 ppm, which were assigned to the E and Z configurations, respectively (**Supplementary Fig. 1b**). The integration gave an E:Z ratio of 96:4. In comparison, the ^{31}P NMR spectrum displayed two signals at 5.51 and 5.58 ppm, with E:Z ratio of 95:5 (**Supplementary Fig. 2**). The consistency in E:Z ratio with E as the dominant configuration confirms FTPA-CPA tends to exhibit E configuration. A similar analysis was also performed on FMTPA-CPA. In both the ^{1}H and ^{31}P NMR spectrum, the E:Z ratios are highly consistent, giving 8:92 and 9:91, respectively (**Supplementary Fig. 5 & 6**). It confirms that free FMTPA-CPA predominantly adopts the Z configuration. These experimental results are consistent with the DFT calculation results.[9]

For molecules anchored on ITO, both FTPA-CPA and FMTPA-CPA exhibit Z configuration. As both FTPA-CPA and FMTPA-CPA are anchored on ITO substrate when applied in pero-SCs, we further compare the total energies of the whole systems composed of both molecules with E (Z) configuration on the ITO substrate (**Supplementary Fig. 10**). The energy differences between E and Z configurations of FTPA-CPA and FMTPA-CPA anchored on ITO are 0.66 eV and 0.51 eV, respectively.[4,5] Consequently, Boltzmann distribution analysis confirms that both FTPA-CPA and

FMTPA-CPA exhibit nearly 100% for Z configuration. We also quantified height and orientation of FTPA-CPA and FMTPA-CPA to define their anchoring configuration. As shown in **Supplementary Fig. 11**, XRR revealed molecular heights of 15.9 Å for FTPA-CPA and 16.9 Å for FMTPA-CPA, which are close to the previously calculated anchoring heights of the energetically favored Z configuration on ITO (15.5 Å for FTPA-CPA and 16.7 Å for FMTPA-CPA).[10] In addition, SFG spectroscopy was used to determine average tilt angle of FTPA-CPA on ITO (**Supplementary Fig. 12**). The measured average tilt angle relative to the substrate normal is ~24°, which is much closer to the calculated value of Z configuration (38°) on ITO rather than E configuration (0°). This result implies the anchored FTPA-CPA is assigned mainly to the Z configuration.[11,12]

Supplementary Note 3. The X-ray reflectivity (XRR) calculation details

X-ray reflectivity (XRR) measurements were used to determine the thickness of anchored SAMs. In **Supplementary Fig. 11**, as the incident angle (2θ) increases, the attenuated reflectivity curve shows an inflection point. Upon magnification, at the inflection point, the thickness (d) of the SAM layer can be calculated using the formula

$$\theta^2 - \alpha_c^2 = m^2 \frac{\lambda}{2d}^2$$

Where (0.325°) is the critical angle for total reflection at the ITO substrate interface, m is the order of diffraction fringes (m=1), and λ (0.15404 nm) is the X-ray wavelength (Cu Kα).

Supplementary Note 4. The Sum Frequency Generation (SFG) calculation details

The visible and infrared beams were focused and superimposed on the quartz/SAM samples in order to generate the SFG signals. An optical parametric generation/amplification and difference frequency generation (OPG/OPA/DFG) system, based on LiB_3O_5 and $AgGaS_2$ crystals, was employed to generate an IR beam with a tunable wavenumber ranging from 1000 to 4300 cm^{-1}. The wavelength of the visible beam was fixed at 532 nm, derived from a Nd:YAG laser. The SFG spectra were collected with the *ssp* and *ppp* (with the letters from left to right representing the polarization of the output SFG field, the input visible and infrared field, respectively) polarization combinations, with a wavenumber step of 5 cm^{-1}. For this vibrational mode, the polarization-dependent effective susceptibilities can be related to the molecular tilt angle θ (between the vibrational axis and the surface normal) by

$$\frac{\chi_{eff,spp}}{\chi_{eff,ppp}} = \frac{0.29 < cos\theta > +0.08 < cos^3\theta >}{0.62 < cos\theta > -0.62 < cos^3\theta >}$$

Where $X_{\text{eff,spp}}$ and $X_{\text{eff,ppp}}$ are the effective macroscopic second-order susceptibility of spp and *ppp* polarization combinations, respectively; The orientational averages are defined as

$$< cos\theta >= \int_0^{\pi} cos\theta f(\theta)\, sin\theta d\theta$$

$$< cos^3\theta >= \int_0^{\pi} cos^3\theta f(\theta)\, sin\theta d\theta$$

Assuming a Gaussian orientational distribution:

$$f(\theta) = Cexp[-\frac{(\theta-\theta_0)^2}{2\sigma^2}]$$

where C is the normalization constant, θ_0 is the average tilt angle, and σ describes the orientational distribution width.

Supplementary Note 5. Ground-state geometry optimizations and radical character analysis

To analyze radical character by theoretical methods, fractional occupation density number (N_{FOD}) was calculated.[13] A larger N_{FOD} indicates obvious radical character. Based on the N_{FOD} analysis, the 2PACz showing very low N_{FOD} (0.10) consistent with negligible radical characteristics in **Supplementary Table 2**. Intermediate values for FTPA-CPA (0.43) suggest moderate radical characteristics, while FMTPA-CPA (0.66) exhibit significantly higher N_{FOD} values, implying stronger radical characteristic.

Fractional occupation density (FOD) analysis was carried out using the ORCA quantum chemistry program package (version 4.2.1).[14] The calculations were performed at the FOD-DFT level employing the TPSS functional in combination with the def2-TZVP basis set. A Fermi-Dirac smearing temperature of 5000 K was applied to introduce fractional occupations, enabling visualization and quantification of static correlation effects and polyradical character.

Supplementary Note 6. DFT calculation of electrostatic surface potential (ESP)

The geometries of the molecules were optimized with the Gaussian 16 software package at the B3LYP/6-31G(d,p) level of theory.[15] The D3(BJ) dispersion correction was included during geometry optimization to better account for long-range intramolecular dispersion interactions. Based on these optimized structures, subsequent analysis of the ESP distribution was conducted using the Multiwfn.[16,17]

Supplementary Note 7. The acid dissociation constant (pKa) calculation

The pKa was calculated by DFT employing ORCA 6.0.1. The calculation details are shown below:

$$pKa = \left[G_{gas}(A^-) + \Delta G_{sol}(A^-) + G_{gas}(H^+) + \Delta G_{sol}(H^+) - G_{gas}(HA) - \Delta G_{sol}(HA)\right]/1.3644$$

where $G_{gas}(A^-)$, $G_{gas}(HA)$ and $G_{gas}(H^+)$ are the represents the gas free energy of

corresponding material. $\Delta G_{sol}(A^-)$, $\Delta G_{sol}(HA)$ and $\Delta G_{sol}(H^+)$ are the represents the solvation free energy of corresponding materials, among that $G_{gas}(H^+)$ and $\Delta G_{sol}(H^+)$ are obtained from experiment data.[18] The gas free energy calculated at B3LYP-D3(BJ)/ma-def2-TZVP//B3LYP-D3(BJ)/def2-SVP level and the solvation free energy was calculated at M052X/6-31G* in SMD solvation model.[19,20]

In this work, the SAMs were prepared using ethanol (EtOH), thus our calculations were performed in EtOH environments, whose lower dielectric constants reduce conjugated base stabilization and thus result in higher apparent pKa values compared with H_2O (**Supplementary Table 6**). For 2PACz, FTPA-CPA and FMTPA-CPA, the substituents (R) attached to the phosphonic group result in charge redistribution, thus having impact on the stability of the deprotonated conjugate base. FMTPA-CPA, which contains D-A-D electronic resonance, shows the lowest pKa (1.66 in H_2O, 5.80 in EtOH) due to resonance enhanced charge redistribution effect. Therefore, both solvent dielectric and molecular substitution groups have large impact on the pKa value of phosphonic acid group in SAMs compared to pristine H_3PO_4. In addition, the acid-base titration results agree well with the computational predictions, with minor deviations within experimental uncertainty (**Supplementary Fig. 18**).

Supplementary Note 8. Molecular Dynamics Simulations

To investigate the self-assembly behavior of SAM molecules on ITO surfaces, we conducted all-atom molecular dynamics (AA-MD) simulations using the GROMACS 2021 software suite, equipped with the General Amber Force Field (GAFF).[21,22]The atom charges were fitted using the Restrained Electrostatic Potential (RESP) method, employing the B3LYP functional and the 6-31G** basis set. All all-atom molecular dynamics simulations were realized in the canonical NVT ensemble at T = 300 K comprising an ITO model system with dimensions 100 Å × 100 Å × 20 Å. Periodic boundary conditions were used in x and y directions. To ensure simulations consistency, the total atom count in each SAM molecular system was standardized to comparable values. The system underwent an initial 10-ns equilibrium simulation, followed by a 10-ns simulated annealing protocol, and concluded with a final 10-ns production simulation. The last 3-ns trajectory was extracted with a sampling interval of 500 femtoseconds (fs) for ensemble average calculations. During the simulations, the LINCS algorithm was utilized to constrain the covalent bonds involving hydrogen atoms.[23] The simulation time step was set to 1.0 fs. Temperature was controlled using the V-rescale thermostat.[24,25] The nonbonded interactions were truncated at a cut-off distance of 12 Å, while the particle mesh Ewald (PME) method was employed to compute long-range electrostatic interactions.[26] Finally, graphics and visualization analyses were handled by the Visual Molecular Dynamics (VMD) program.[27]

To quantitatively analyze the surface coverage of SAM molecules on ITO surfaces, a spatial discretization method was employed. The ITO surface was partitioned into discrete grid cells. For each cell, the presence or absence of SAM molecules was recorded statistically. The surface coverage of SAM molecules was then calculated by dividing the number of grid cells containing SAM molecules by the total number of

partitioned cells. The fraction of surface coverage (θ) is defined as:

$$\boldsymbol{\theta} = \frac{N_{SAM}}{N_{gri}}$$

Where θ is the fraction of Surface coverage of SAM molecules, N_{SAM} is the number of grid cells containing SAM molecules, N_{gri} is the total number of grid cells partitioning the ITO surface.

Supplementary Note 9. DFT calculation of the binding energy (E_b)

First-principles calculations were conducted within the framework of density functional theory (DFT),[28] as implemented in the Vienna Ab initio Simulation Package (VASP) code.[29,30] The projector augmented wave (PAW) method was employed to describe core-valence interactions, utilizing a plane-wave basis set with a kinetic energy cutoff of 450 eV. The generalized gradient approximation exchange-correction functional formulated by Perdew, Burke, and Ernzerhof (PBE)[31] is used in all calculations. Single Γ point was used in all calculations for Brillouin zone sampling. An In_2O_3 (111) plane served as the model for the ITO substrate, onto which 2PACz, FTPA-CPA, and FMTPA-CPA molecules were subsequently adsorbed with an upward orientation. The electronic configurations for In, O, C, N, P, F, and H elements are $4d^{10}5s^25p^1$, $2s^22p^4$, $2s^22p^2$, $2s^22p^3$, $3s^23p^3$, $2s^22p^5$ and $1s^1$. The vdW interactions were incorporated into the geometrical optimization process using the DFT-D3 method,[30] with residual forces on atoms converged below 0.05 eV/Å. During this process, all substrate atoms except those on the surface were fixed. The self-consistent field calculations were performed using the convergence criterion of 10^{-5} eV/atom. The formula for calculating the binding energy (E_b) of a SAM adsorbed on the substrate is

$$E_b = E_{ITO+SA} - E_{ITO} - E_{SAM(-2H)}$$

where $E_{ITO+SAM}$ represents the total energy of the SAM adsorbed on the ITO substrate, E_{ITO} is the total energy of the ITO substrate, and $E_{SAM(-2H)}$ is the energy of the SAM after the removal of two hydrogen atoms from its anchoring group.

Supplementary Note 10. The initial aggregate of 2PACz, FTPA-CPA and FMTPA-CPA

During the device fabrication process, EtOH washing was applied to minimize the formation of multilayer structures or molecular aggregates. Ethanol soaking, and AcOH washing were further applied to remove weakly bound aggregates. As shown in **Supplementary Fig. 20-22 & Table 7**, the high P/In (0.023) of FMTPA-CPA has negligible change, whereas those of 2PACz (from 0.011 to 0.007, 0.006 and 0.004) and FTPA-CPA (from 0.016 to 0.014, 0.013 and 0.007) significantly decreased. This indicates that FMTPA-CPA majorly forms the stable covalent anchored monolayer after EtOH washing, while 2PACz and FTPA-CPA samples initially contain a tiny amount of multilayer or aggregated molecules.

Supplementary Note 11. The energetic disorders and analysis of dynamic energetic disorder

For 2PACz, the strong π-π interactions between the carbazole cores lead to large binding energies in dimer formation and highly disordered aggregation. The calculated static energetic disorder is the highest among the studied molecules (0.297 eV, **Supplementary Fig. 52**), and AFM-IR together with SECCM-TLCV results confirm its inhomogeneous surface coverage (**Supplementary Fig. 23 & 33**). In addition, MD-DFT simulations indicate locally strong intermolecular electronic coupling within aggregated dimers but negligible coupling in uncovered regions (**Supplementary Fig. 53**). This spatially heterogeneous coupling interrupts charge-transport continuity; despite locally favorable interaction, the overall charge-transport connectivity remains limited. Consequently, 2PACz exhibits the strongest temperature dependence of hole conductivity due to its high energetic disorder.

In contrast, the D-A-D electronic resonance FMTPA-CPA enhances anchoring strength, indicating an extremely weak tendency to aggregate. The energetic disorder is the lowest (0.190 eV, **Supplementary Fig. 52**), and AFM-IR and SECCM-TLCV confirm the compact and homogeneous coverage across the ITO substrate as shown in **Fig. 3c & Supplementary Fig. 23 & Fig. 33**. Consequently, the electronic resonance FMTPA-CPA shows uniform and ordered molecular arrangement, thus exhibiting the weakest temperature dependence of hole conductivity. MD-DFT results also reveal that although FMTPA-CPA possesses moderate intermolecular coupling in **Supplementary Fig. 52**, its uniform molecular arrangement enables well-connected transport pathways, minimizing trap formation and maintaining efficient hole conduction. This combination of homogeneous packing and sufficient coupling ensures efficient hole conductivity and weaker temperature dependence.

In addition to static energetic disorder and intermolecular electronic coupling, temperature dependence of electronic conductivity also strongly depends on the extent of intramolecular dynamic energetic disorder quantified by intramolecular structural reorganization energy.[32] Here, we calculated the intramolecular structural reorganization energies (λ) of FTPA-CPA and FMTPA-CPA for hole transport, 0.33 and 0.20 eV, respectively. Much larger λ values and static energetic disorder (σ) values than intermolecular electronic coupling values (see **Supplementary Fig. 52**) lead to localized hole-transport states, which has been well known in charge-transport research filed.[32] In such cases, charge transport predominantly proceeds through thermally activated hopping between these localized states, which can usually be described in the framework of Marcus electron-transfer theory. At low temperatures, the hopping rate is suppressed because carriers lack sufficient energy to overcome the potential barriers between neighboring localized states, leading to reduced conductivity. As the temperature increases, thermal activation facilitates more frequent hops, resulting in enhanced hole conductivity.[32] Therefore, the thermally activated temperature dependences observed for FTPA-CPA and FMTPA-CPA are consistent with a hopping-type transport mechanism associated with localized charge-transport states.

As shown by the results of our ESR measurements and DFT calculations, FTPA-CPA and FMTPA-CPA possess radical character to some extent. Importantly, the electronic resonance in FMTPA-CPA not only gives rise to a stronger radical character, but also leads to the HOMO delocalization on the two donor moieties. Therefore, the λ value of FMTPA-CPA is significantly reduced compared to that of FTPA-CPA. As shown in **Supplementary Fig. 53**, FTPA-CPA, exhibiting higher dynamic energetic disorder (due to a larger reorganization energy of 0.33 eV, **Supplementary Fig. 54**), possesses more localized states and thus higher activation barriers for charge hopping. Consequently, the conduction in FTPA-CPA is more thermally activated, showing stronger temperature dependence. In contrast, FMTPA-CPA has a smaller reorganization energy (0.20 eV, **Supplementary Fig. 54**) and a much narrower energetic distribution due to its homogeneous, stable molecular arrangement. Although its transport still follows a hopping mechanism, the uniform arrangement reduces trapping and energy barrier, enabling efficient hopping even at lower temperatures. As a result, FMTPA-CPA exhibits weaker temperature dependence of hole conductivity.

Supplementary Note 12. Electrochemical measurement details

Quartz capillaries (I.D./O.D., 0.7/1.0 mm) were drawn into micropipettes with a diameter of 20 μm using an ultra-high temperature puller (MT-PULLER100A). In the SECCM-TLCV experiment, ITO/SAM was used as ITO/SAM was used as the working electrode (WE), Ag wire served as the quasi-reference-counter (QRCE), and a quartz micropipette filled with 0.1 M TBAP in ACN was employed as the SECCM probe. To carry out the SECCM-TLCV experiment, the quartz micropipette with the meniscus was moved to approximately 30 μm above the ITO/SAM. The threshold for surface current feedback is set at 120% to determine when the meniscus contacts the surface of the WE and to stop further movement. Local-CV curves were recorded within the hemispherical droplet formed between the SECCM tip and the WE surface. SECCM images (80 × 80 μm^2 scan area) obtained with the voltametric hopping mode "SECCM + local-CV" protocol, visualizing assembly density distribution of SAMs on ITO.

All localized micro-area electrochemical measurements were conducted using a super-resolution electrochemical microscopy system, with SPRM v1.0 software provided by MinTech (MT-SRECM300 Pro, CAS Applied Chemistry Science & Technology Co. Ltd., Changchun). The experimental setup was installed inside a Faraday cage and placed on a pneumatic damping antivibration platform.

Assembly density (Γ_0) of the SAMs was calculated according to the CV data.

$$\Gamma_0 = \frac{Q}{nFA}$$

Where Q is the integrated charge, n is the electron transfer number for SAMs oxidation, F is the Faraday constant, and A is the geometric area of WE.

Supplementary Note 13. the stability of combined environment of light including UV and heat

We evaluate stability under UV-inclusive light (metal halide (MH), 100 mW cm^{-2}, 4.4% UV inside, the spectrum in **Supplementary Fig. 64**). The FMTPA-CPA-based device maintains 97% of its initial efficiency after continuous MPPT for 1,080 h, while the FTPA-CPA and 2PACz-based devices retain only 84% and 46% after 600 h (**Supplementary Fig. 65**).

We also evaluate device stability under a combined environment of UV-inclusive light and heat (85±5ºC) as shown in **Supplementary Fig. 66**. The maximum-power-point tracking (MPPT) tests were conducted under 100 mW cm^{-2} LEP light (1.4% UV inside, the spectrum is shown in **Supplementary Fig. 64a** exposure at 85±5ºC in N_2 atmosphere, with the FMTPA-CPA-based device maintains 95% of its initial efficiency during continuous MPPT for 1,080 h, whereas the 2PACz-based and FTPA-CPA-based devices fall to below 44% and 80% of their initial efficiency after 600 h (**Supplementary Fig. 66a**). These UV-inclusive light and heat stability results are comparable with the state-of-the-art results,[33] demonstrating the practical durability of devices using the D-A-D resonant SAM.

Furthermore, to demonstrate the industrialization potential of our D-A-D resonant SAM, we evaluate the stability measurements on modules (aperture area of 15.64 cm^2) under combined environment of light including UV (MH (4.4% UV inside)) and heat (85±5 ºC). The FMTPA-CPA-based module maintains ~90% of its initial efficiency after continuous maximum-power-point tracking (MPPT) for 1,080 h, whereas the FTPA-CPA-based and 2PACz-based modules fall to below ~73% and ~28% of their initial efficiency after 900 h (**Supplementary Fig. 67**).

Supplementary Note 14. Stability Mechanism Analysis

With more detailed investigations, we prefer to ascribed the covalent P-O-In bond cleavage to the thermally activated hydrolysis, where the P-O-In bond was attacked by the protons released from organic cations in perovskite.

To verify the complex degradation mechanism, we firstly check the intrinsic stability of anchored reference SAMs. We prepared 2PACz films with EtOH washing, which were subjected to five accelerated aging conditions, including high temperature (85 ± 5 ℃ for 1000 h), light illumination (1000 h), electrical bias stressing (−2.0 V for 10 h), high humidity (85±5% RH for 1000 h), and bending stress (10000 cycles, 5 mm radius). After these accelerated aging tests, XPS characterization revealed no significant changes in **Supplementary Fig. 71**, indicating environmental stability of the pristine 2PACz films.

Based on this, the failure mechanism of the reference SAMs should have strong relation with the perovskite layer. We further prepared 2PACz and FTPA-CPA films (still using EtOH washing to avoid weakly bonded aggregates) with PbI_2 deposition, formamidinium iodide (FAI) deposition and AcOH soaking, respectively, followed by 1000 h of thermal aging in N_2 atmosphere. The 2PACz and FTPA-CPA samples with PbI_2 layer on top showed negligible changes. The P/In signal ratios of 2PACz and FTPA-CPA decreased markedly with FAI film deposition, and the SAMs desorption is

even more severe after AcOH soaking in **Supplementary Fig. 72 & Fig. 73**. Considering both FAI and AcOH can provide proton during long-term heat treatment, these results indicate that protonic attack under thermal play a key role in activating P-O-In bond cleavage. In contrast, the P/In ratio of FMTPA-CPA remains nearly unchanged under all aging conditions in **Supplementary Fig. 72**, confirming that its D-A-D electronic resonance fundamentally reinforces the P-O-In bond strength.

As the analysis above, we attribute the failure mechanism of P-O-In bond cleavage to thermally activated hydrolysis. During device operation, perovskite degradation can release protonic species (H^+, NH_4^+, or other proton) from FA^+/MA^+ cations.[34,35] Once accumulated at the ITO substrate, the protonic readily attack the electrophilic P-O moiety in the anchoring group, resulting in protonation of the bridging oxygen and subsequent hydrolytic cleavage of the P-O-In bonds.[36-38] With the covalent binding energy of −2.31 eV between FMTPA-CPA and ITO, the P-O-In bond is strong enough to suppress proton attack. With a covalent binding energy of −2.31 eV (similar to that of FMTPA-CPA anchoring on ITO), the P-O-In bond is strong enough to avoid dissociation during practical operation.

$$\text{P-O-In} + H^+ \rightarrow \text{P-OH}^+\text{-O-In} \rightarrow \text{P-OH} + \text{In-OH}$$

To verify the UV degradation mechanism, we prepared ITO/SAM (with EtOH washing)/perovskite samples. As shown in **Supplementary Note 10**, after EtOH washing, the initial coverage of 2PACz and FTPA-CPA may include a certain amount of weak hydrogen-bonded SAMs due to the severe molecular aggregation, and the D-A-D resonant FMTPA-CPA tends to form uniform and covalently anchored monolayer. Then, these samples were aged under metal halide (MH, 4.4% UV inside) lamp and pure UV (365 nm, 56 mW cm^{-2}) lamp, respectively. As for 2PACz and FTPA-CPA, the perovskite buried interfaces showed increased voids and decreased PL intensity after aged 200 h under MH lamp (**Supplementary Fig. 74 & 75**). The significant change is ascribed to weak hydrogen-bonded SAM anchored on ITO, which is triggered by photochemical reaction involving the reaction between deprotonated hydrogen from CPA group with formamidinium cation (FA^+) or iodide anion (I^-), thereby promoting degradation of the buried perovskite interface.[33] In contrast, the perovskite buried interface based on FMTPA-CPA showed only minimal differences, indicating that the robust and stable covalent anchoring of D-A-D resonant FMTPA-CPA will not be influenced by UV photochemical degradation pathway.

Furthermore, we investigate the degradation mechanism after 200 h aging under pure UV (365 nm, 56 mW cm^{-2}) lamp. As for 2PACz and FTPA-CPA, the buried interface degradation became much more severe than that under MH lamp (**Supplementary Fig. 76 & 77**), as evidenced by increased voids, the appearance of bright crystals (referring to PbI_2), and decreased PL intensity. In addition, the PL peaks exhibited a blue shift, which was ascribed to ion migration of A-site cations (e.g., Cs^+, FA^+) that induces weak phase segregation.[39] These results indicate that under harsher pure UV irradiation, the degradation is not only limited to photochemical desorption of weakly hydrogen-bonded SAMs, but also involves UV-induced defects generation and ion migration

within the perovskite bulk. Similarly, the FMTPA-CPA-based buried perovskite interfaces also exhibited bright crystals formation, accompanied by PL intensity decrease and peak blue shift. However, after pure UV lamp aging, the P/In ratio of FMTPA-CPA anchored on ITO showed no significant change from XPS characterization in **Supplementary Fig. 78** and **Supplementary Table 8**. Therefore, we attribute the degradation mainly to UV-induced defects generation and phase segregation in the perovskite bulk, rather than desorption of the FMTPA-CPA SAM itself.

Supplementary Figures

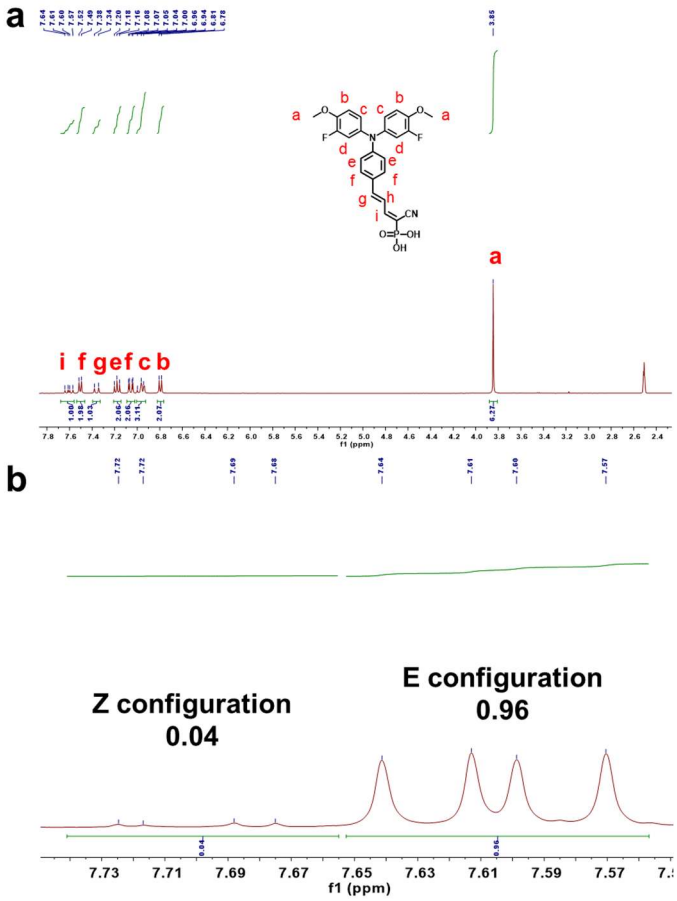

Supplementary Fig. 1 (a) ^{1}H NMR spectrum of FTPA-CPA; (b) enlarged ^{1}H NMR spectrum in the range of 7.56~7.74 ppm.

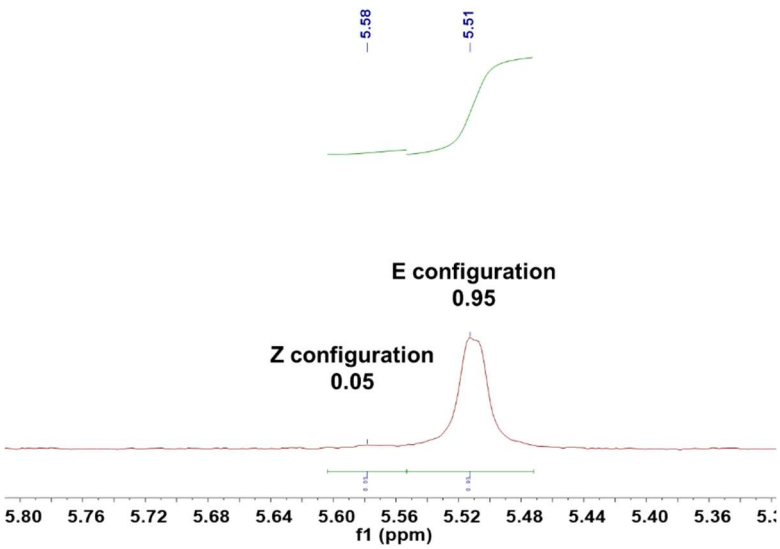

Supplementary Fig. 2 ^{31}P NMR spectrum of FTPA-CPA.

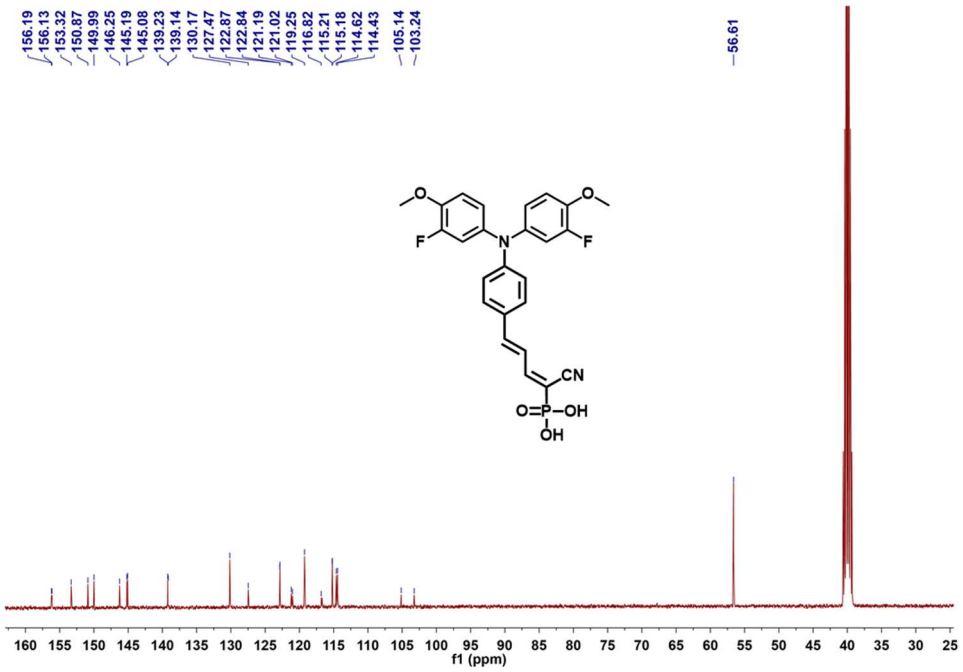

Supplementary Fig. 3 ^{13}C NMR spectrum of FTPA-CPA.

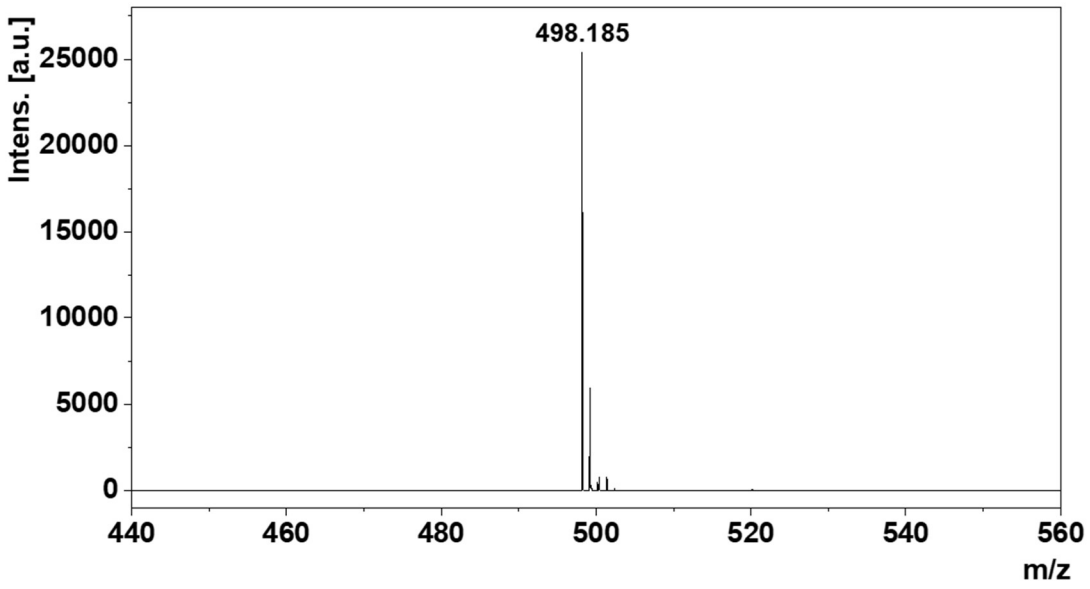

Supplementary Fig. 4 Mass spectroscopy of FTPA-CPA.

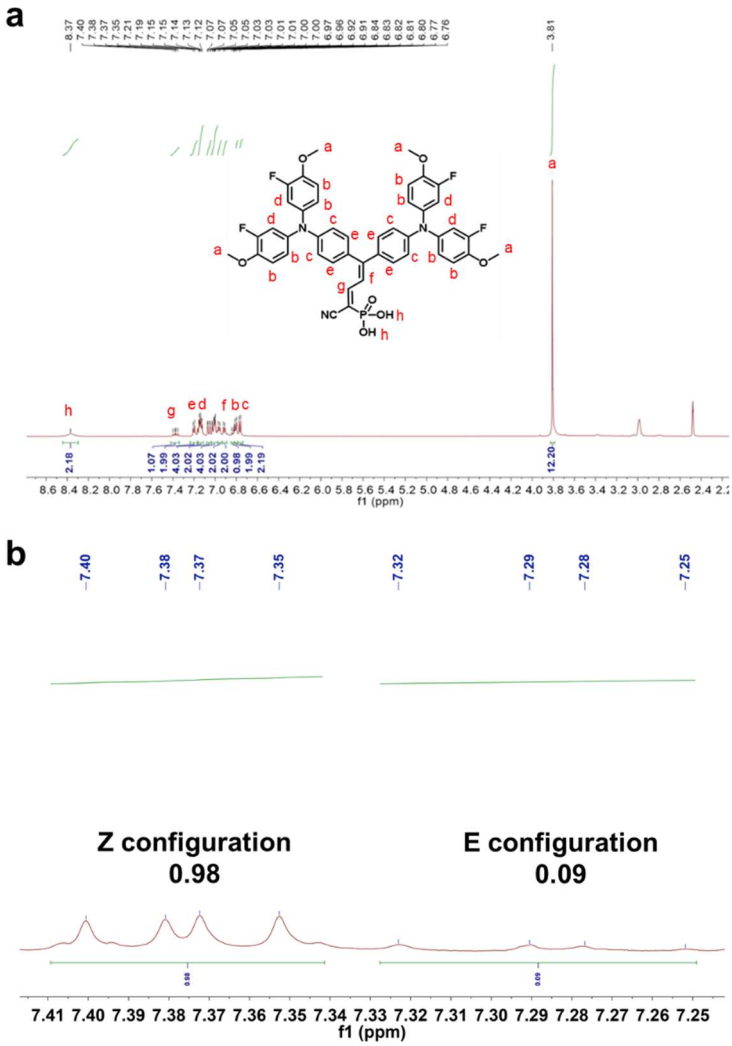

Supplementary Fig. 5 (a) ^{1}H NMR spectrum of FMTPA-CPA; (b) enlarged ^{1}H NMR spectrum in the range of 7.25~7.41 ppm.

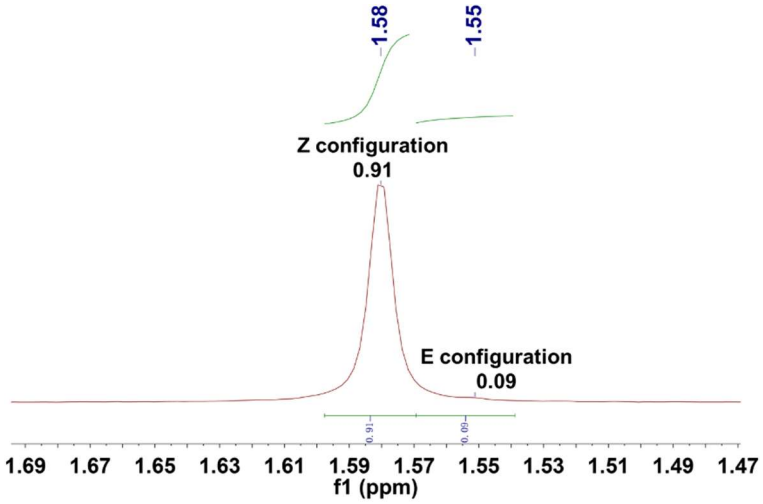

Supplementary Fig. 6 ^{31}P NMR spectrum of FMTPA-CPA.

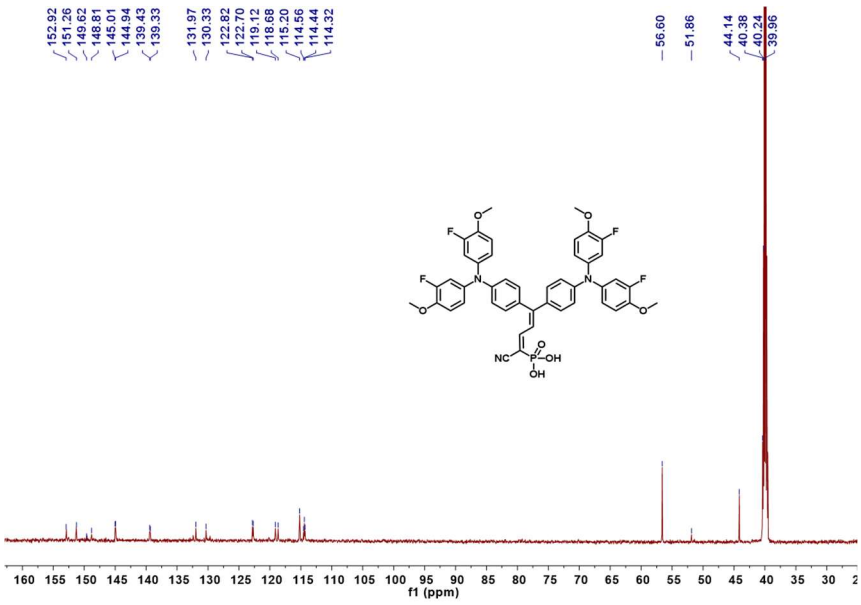

Supplementary Fig. 7 ^{13}C NMR spectrum of FMTPA-CPA.

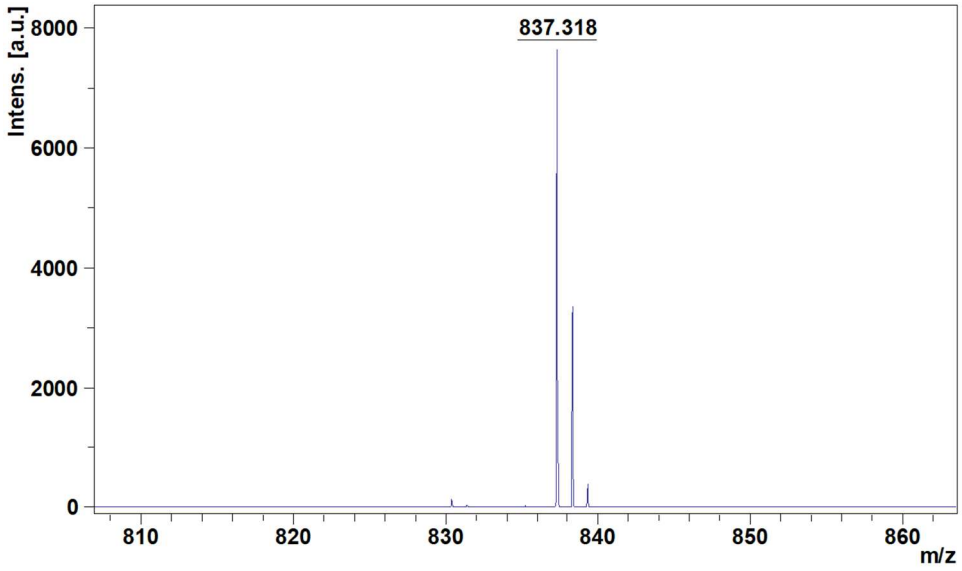

Supplementary Fig. 8 Mass spectroscopy of FMTPA-CPA.

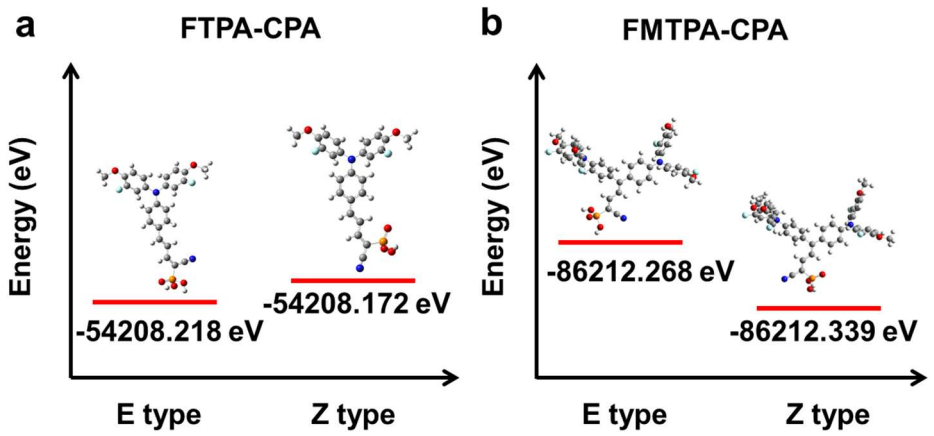

Supplementary Fig. 9 The intrinsic molecular energies of free (a) FTPA-CPA and (b) FMTPA-CPA molecules with E(Z) configuration.

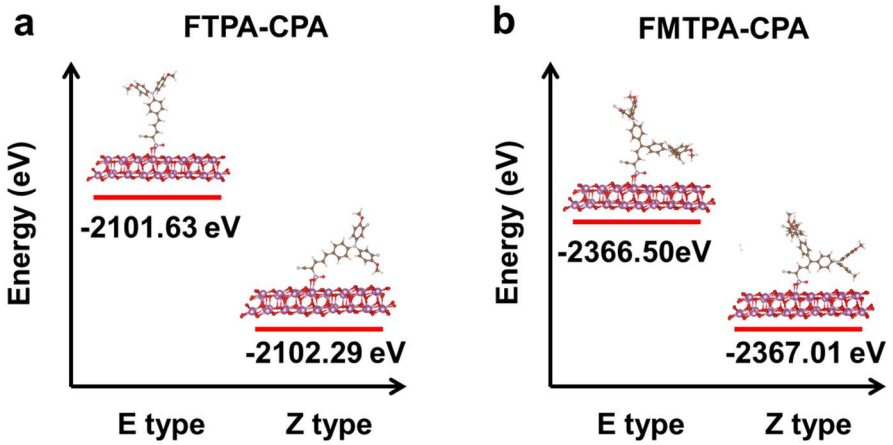

Supplementary Fig. 10 The total energies of the whole systems composed of (a) FTPA-CPA and (b) FMTPA-CPA with E (Z) configuration on the ITO substrate.

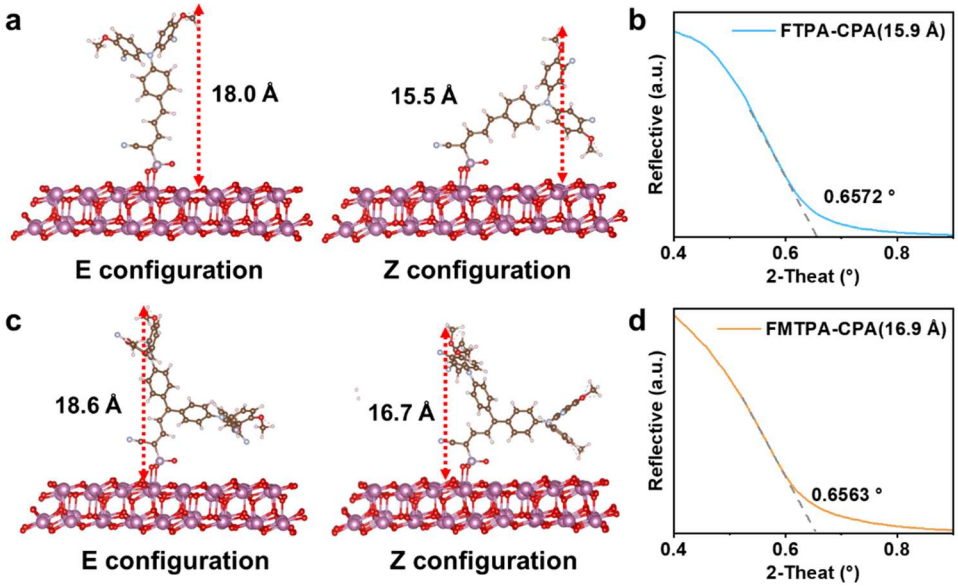

Supplementary Fig. 11 (a) theoretical calculated lengths for E- and Z- configurations FTPA-CPA anchored to ITO; (b) XRR measurements of FTPA-CPA SAM films after AcOH washing; (c) theoretical calculated lengths for E- and Z- configurations FMTPA-CPA anchored to ITO; (d) XRR measurements of FMTPA-CPA SAM films after AcOH washing.

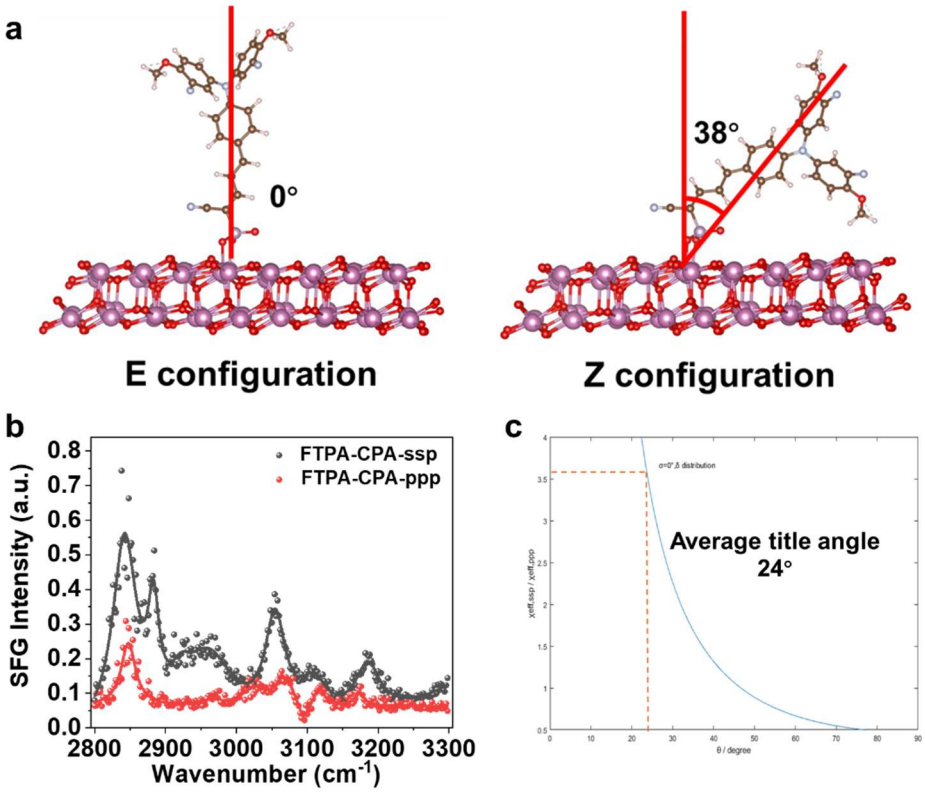

Supplementary Fig. 12 (a) theoretically calculated tilt angle for E- and Z-configurations FTPA-CPA anchored to ITO; (b) the SFG spectra of the FTPA-CPA SAM films after AcOH washing; (c) the predicted average title angle of FTPA-CPA SAMs on ITO by SFG spectra.

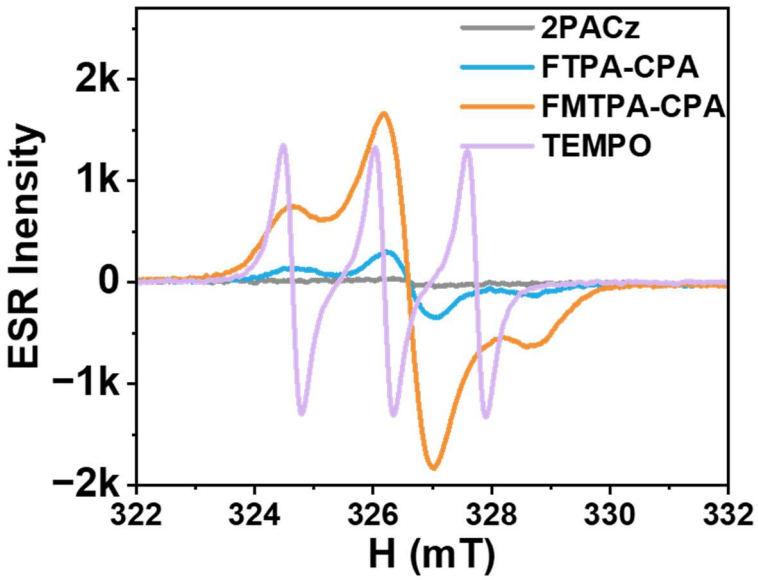

Supplementary Fig. 13 Quantitative ESR spectra of 2PACz, FTPA-CPA and FMTPA-CPA powder.

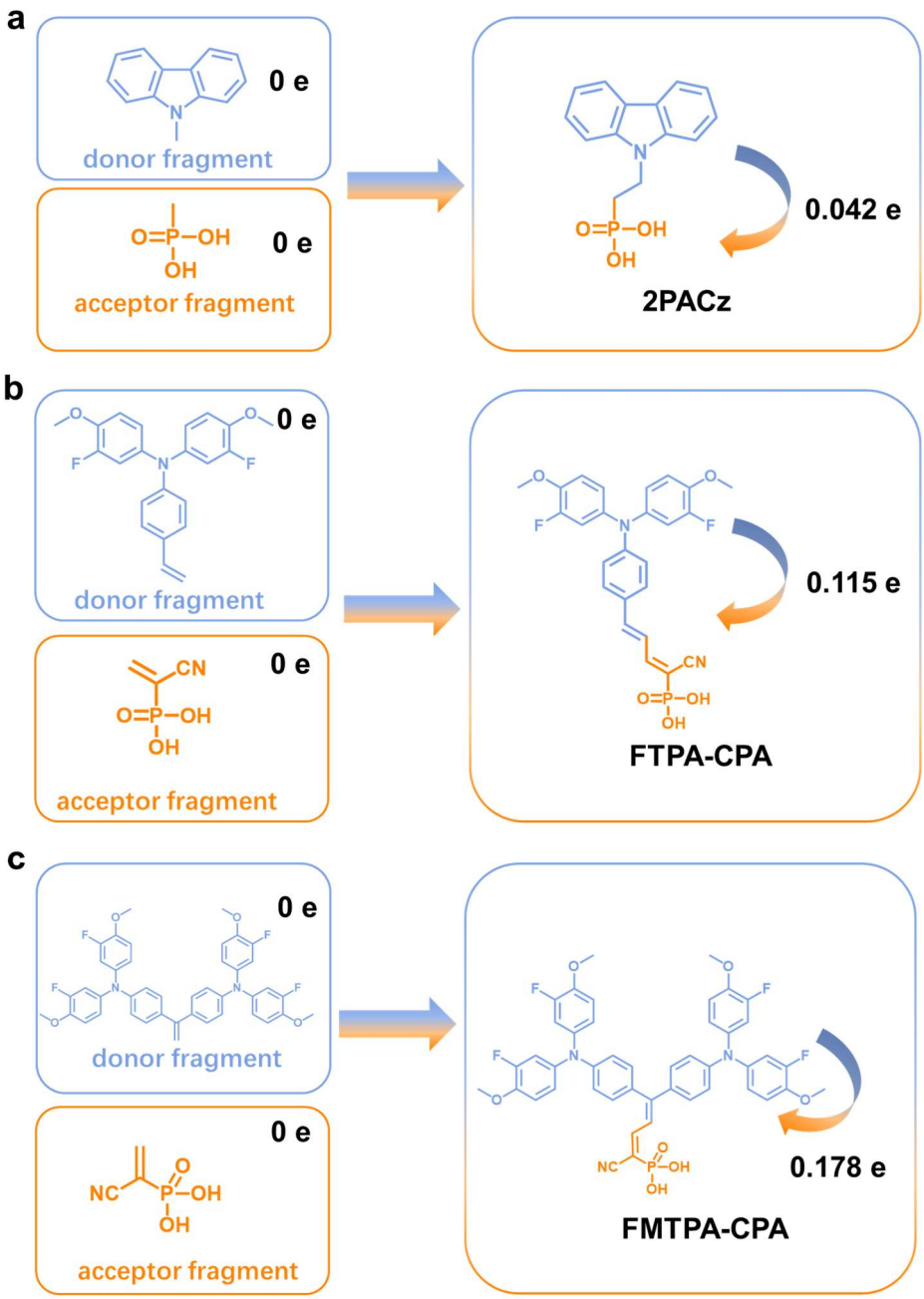

Supplementary Fig. 14 The donor and acceptor fragmentation charges of (a) 2PACz, (b) FTPA-CPA and (c) FMTPA-CPA.

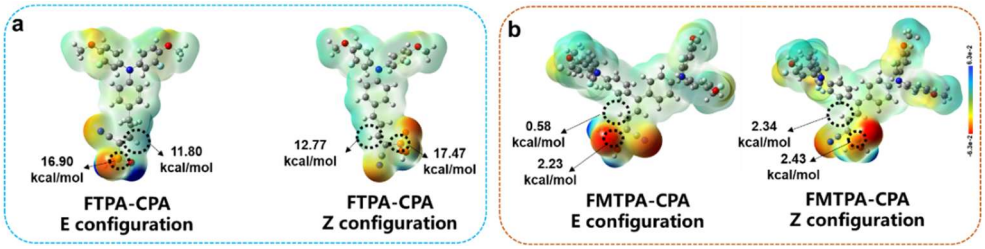

Supplementary Fig. 15 ESP distributions of E and Z configuration (a) FTPA-CPA and (b) FMTPA-CPA.

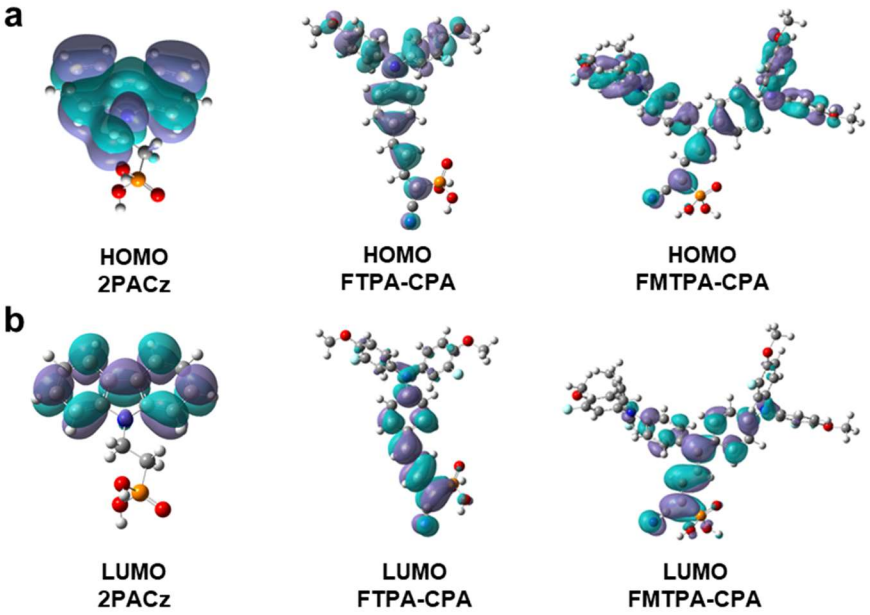

Supplementary Fig. 16 (a) HOMO and (b) LUMO orbital wavefunctions of 2PACz, FTPA-CPA and FMTPA-CPA at the ground-state.

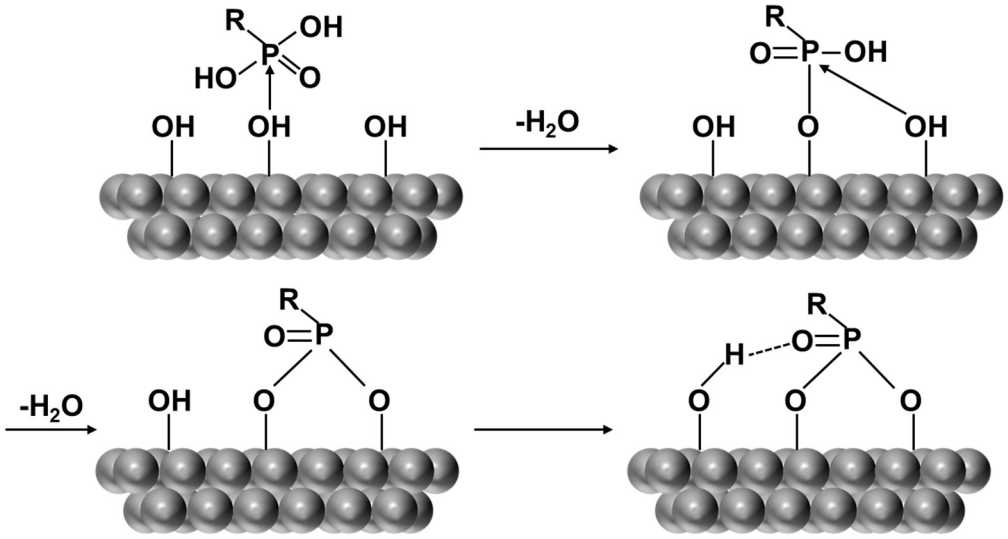

Supplementary Fig. 17 The bonding mechanisms of -PO_3H_2 as anchors on ITO substrates.

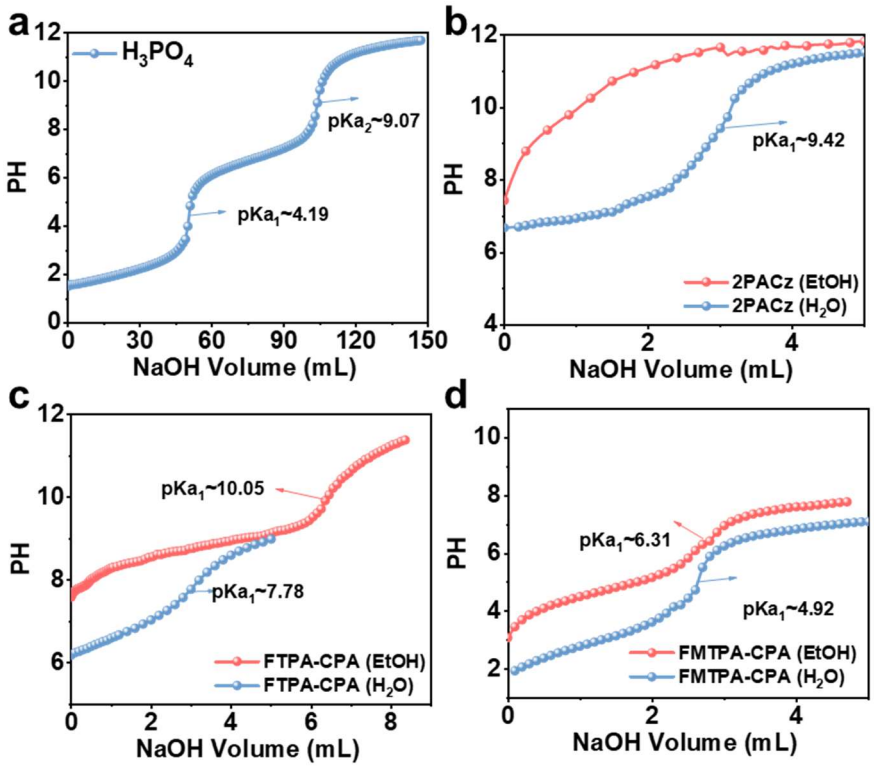

Supplementary Fig. 18 The acid-base titration curve of (a) H_3PO_4, (b) 2PACz, (c) FTPA-CPA and (d) FMTPA-CPA.

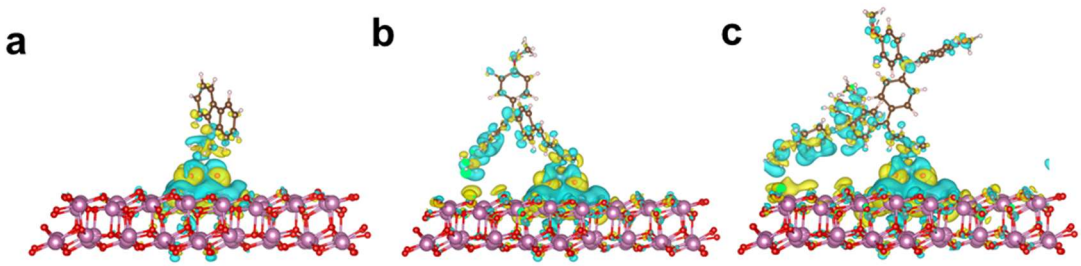

Supplementary Fig. 19 DFT calculation of the binding energies of (a) 2PACz, (b) FTPA-CPA and (c) FMTPA-CPA with ITO.

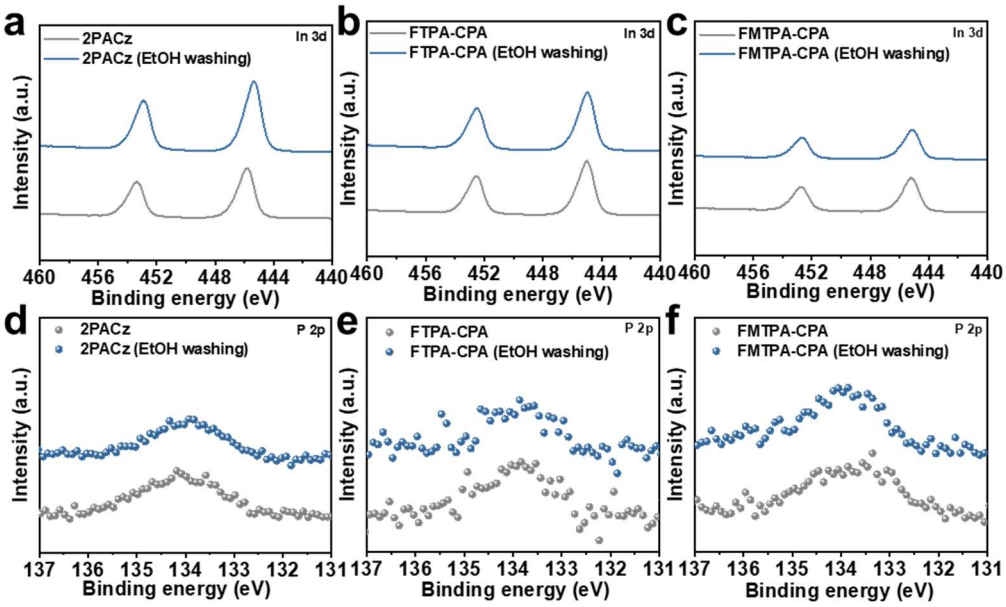

Supplementary Fig. 20 XPS spectra of In 3d obtained from the (a) 2PACz, (b) FTPA-CPA and (c) FMTPA-CPA films before and after EtOH washing; XPS spectra of P 2p obtained from the (d) 2PACz, (e) FTPA-CPA and (f) FMTPA-CPA films before and after EtOH washing.

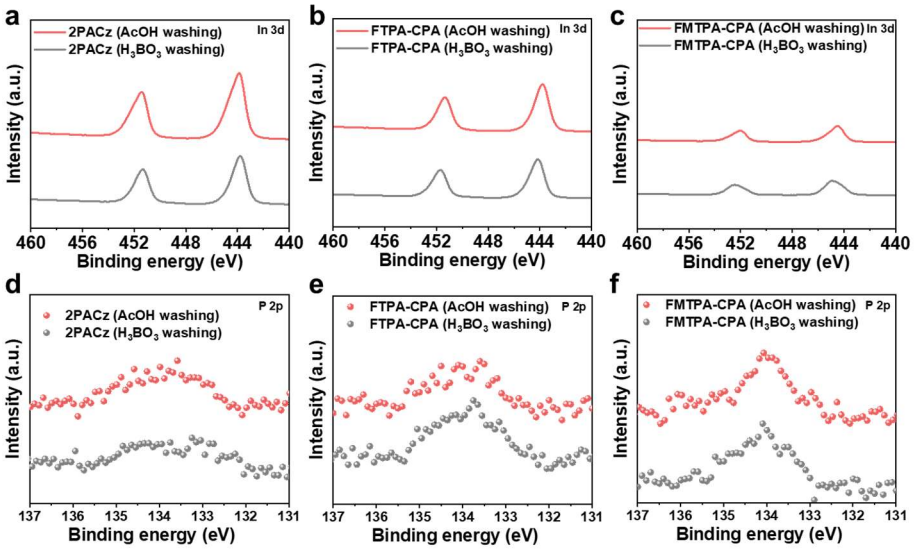

Supplementary Fig. 21 XPS spectra of In 3d obtained from the (a) 2PACz, (b) FTPA-CPA and (c) FMTPA-CPA films after H_3BO_3 and AcOH washing; XPS spectra of P 2p obtained from the (d) 2PACz, (e) FTPA-CPA and (f) FMTPA-CPA films after H_3BO_3 and AcOH washing.

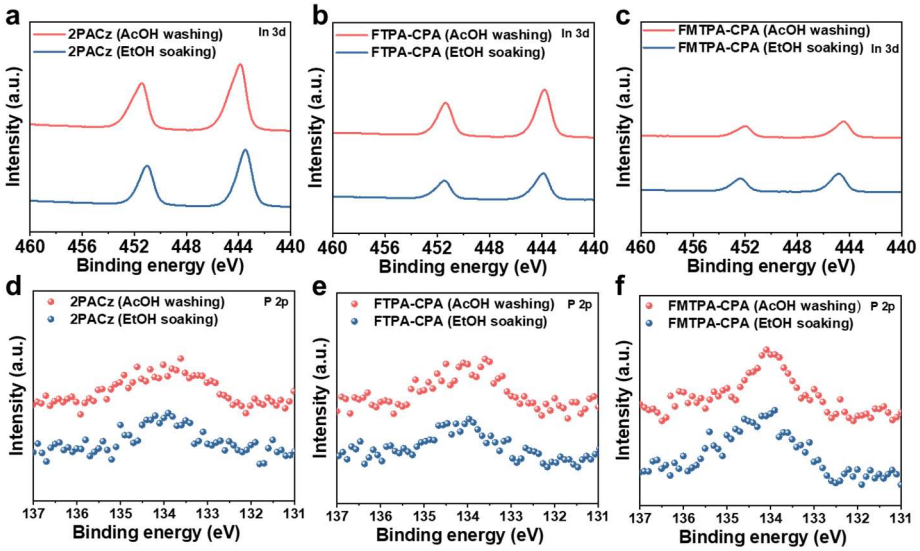

Supplementary Fig. 22 XPS spectra of In 3d obtained from the (a) 2PACz, (b) FTPA-CPA and (c) FMTPA-CPA films after EtOH soaking and AcOH washing; XPS spectra of P 2p obtained from the (d) 2PACz, (e) FTPA-CPA and (f) FMTPA-CPA films after EtOH soaking and AcOH washing.

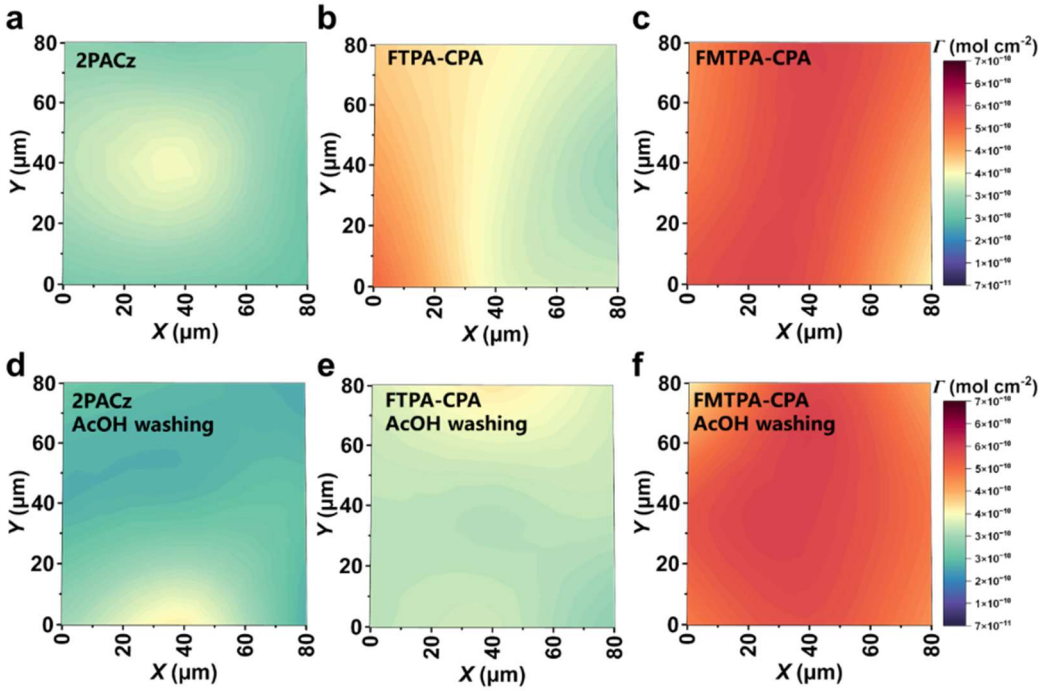

Supplementary Fig. 23 Assembly densities mapping of (a) 2PACz, (b) FTPA-CPA and (c) FMTPA-CPA obtained from SECCM-TLCV. Assembly densities mapping of (d) 2PACz, (e) FTPA-CPA and (f) FMTPA-CPA after AcOH washing obtained from SECCM-TLCV.

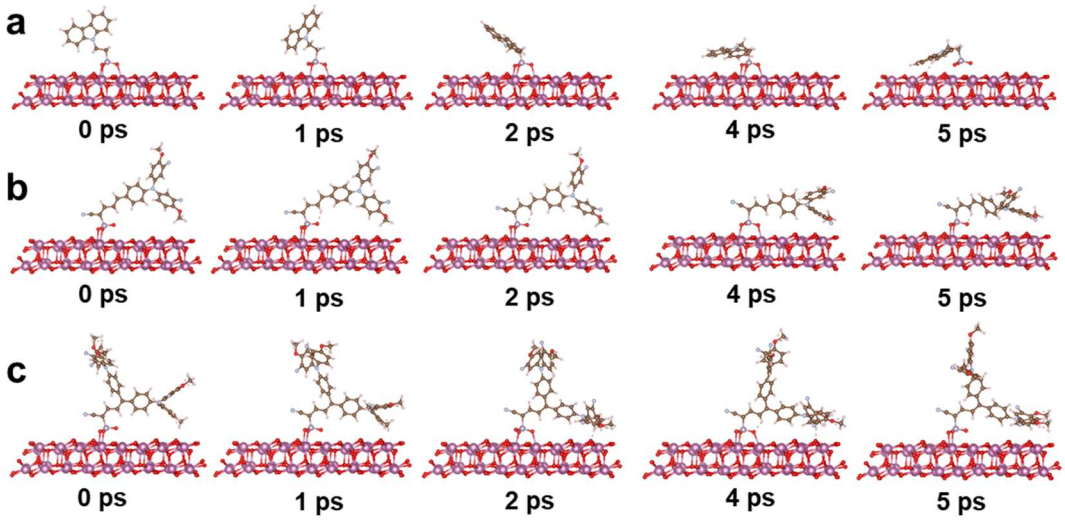

Supplementary Fig. 24 Molecular configuration and anchoring modes of (a) 2PACz, (b) FTPA-CPA and (c) FMTPA-CPA with ITO at 358 K over a span of 0~5 ps.

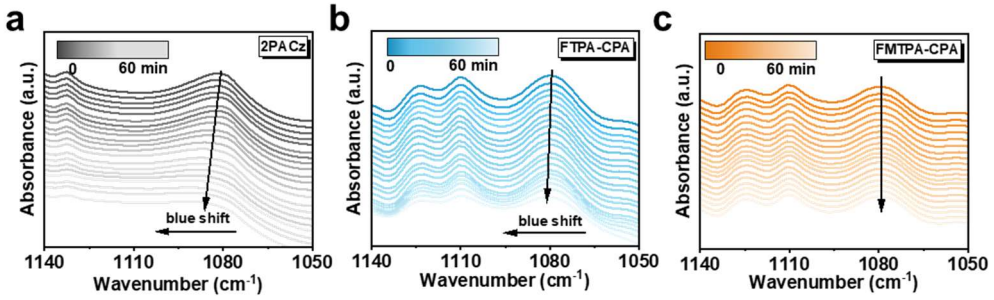

Supplementary Fig. 25 *In situ* FTIR spectra of the (a) 2PACz, (b) FTPA-CPA and (c) FMTPA-CPA films with EtOH washing on ITO substrate at 85 ℃.

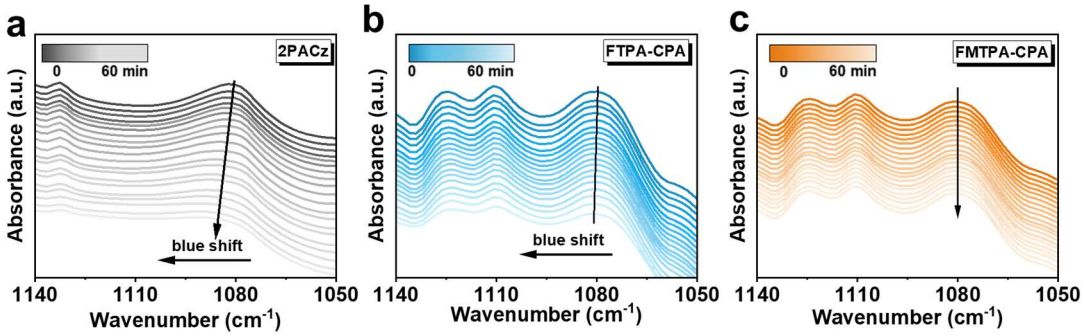

Supplementary Fig. 26 *In situ* FTIR spectra of the (a) 2PACz, (b) FTPA-CPA and (c) FMTPA-CPA films with EtOH washing on ITO substrate at 100 ℃.

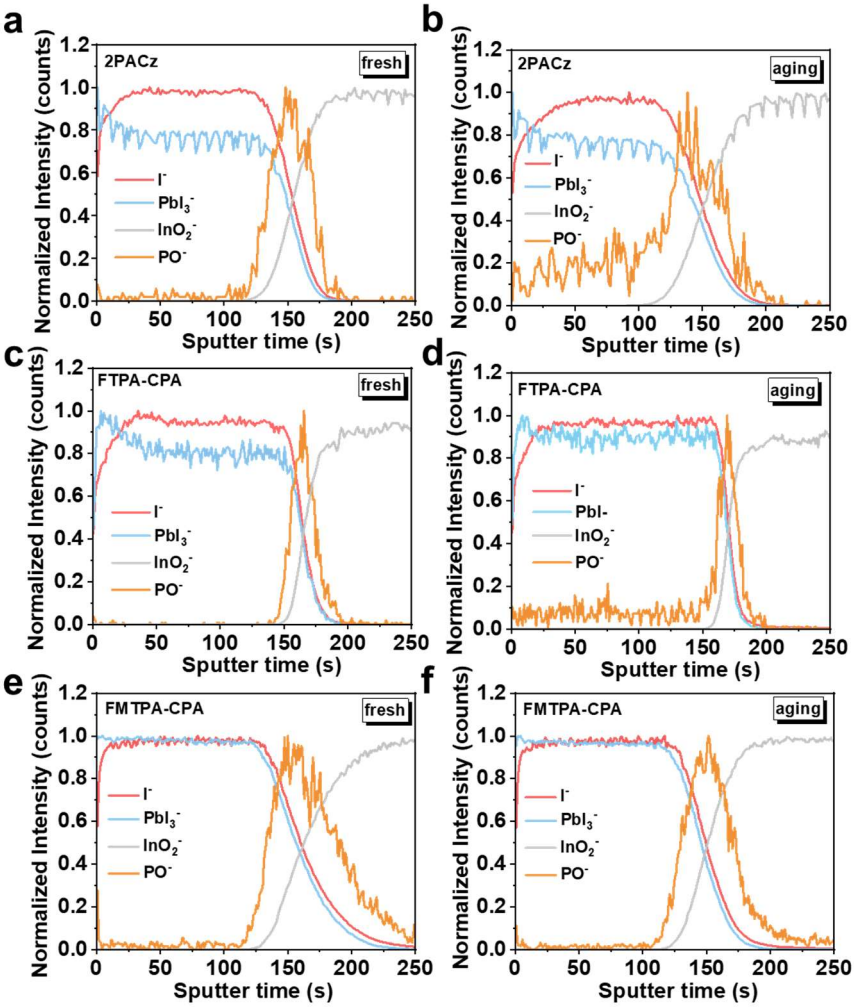

Supplementary Fig. 27 ToF-SIMS depth profiles of 2PACz (a) before and (b) after aging under high temperature and illumination conditions; ToF-SIMS depth profiles of FTPA-CPA (c) before and (d) after aging under high temperature and illumination conditions; ToF-SIMS depth profiles of FMTPA-CPA (e) before and (f) after aging under high temperature and illumination conditions.

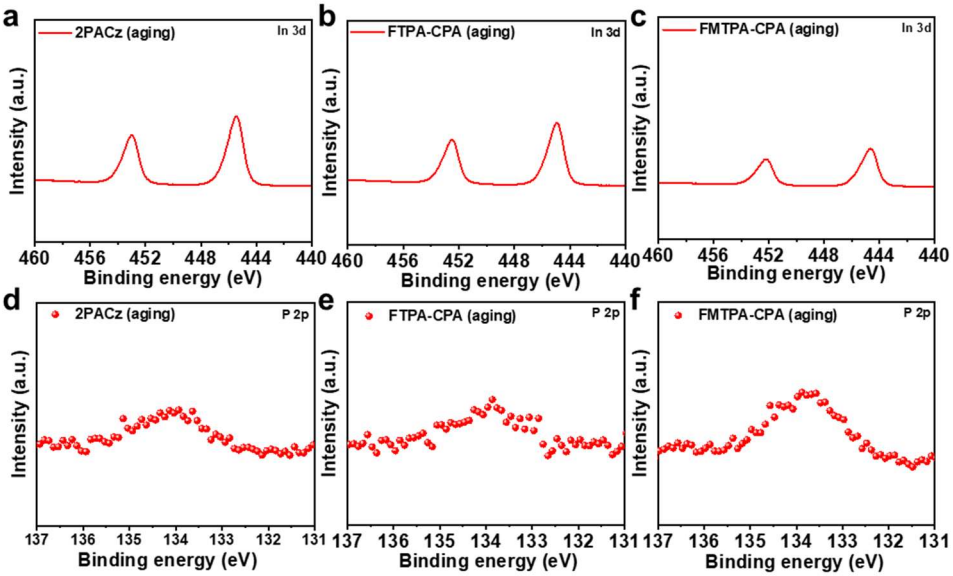

Supplementary Fig. 28 XPS spectra of In 3d obtained from the (a) 2PACz, (b) FTPA-CPA and (c) FMTPA-CPA films after aging under high temperature and illumination conditions; XPS spectra of P 2p obtained from the (d) 2PACz, (e) FTPA-CPA and (f) FMTPA-CPA films after aging under high temperature and illumination conditions.

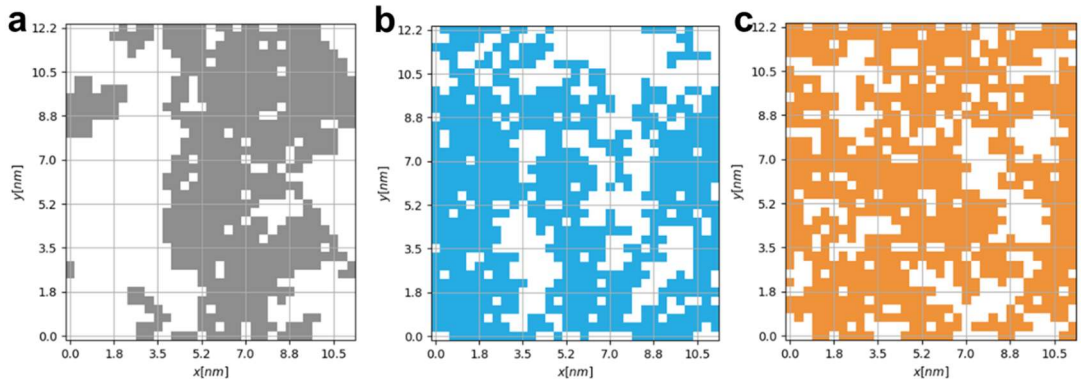

Supplementary Fig. 29 Discretized Grid Distribution Map of (a) 2PACz, (b) FTPA-CPA and (c) FMTPA-CPA SAMs on ITO substrate surface.

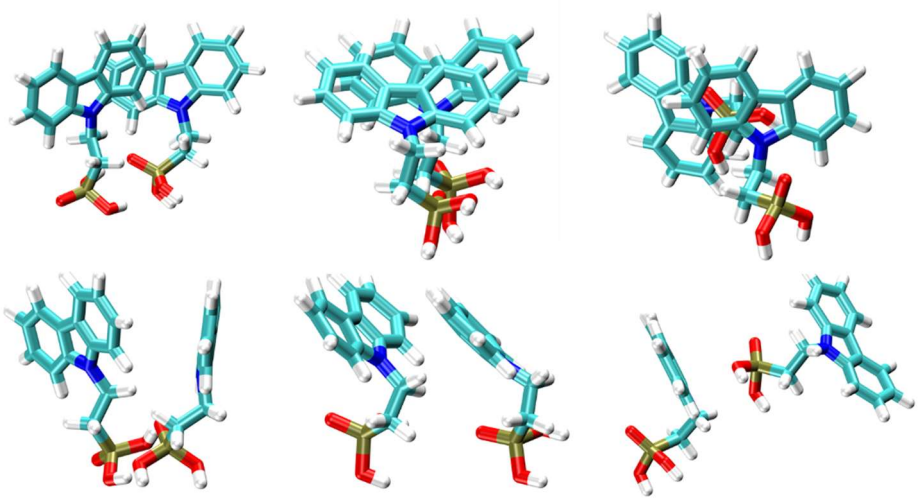

Supplementary Fig. 30 2PACz dimer packing conformation diagram observed in MD simulations.

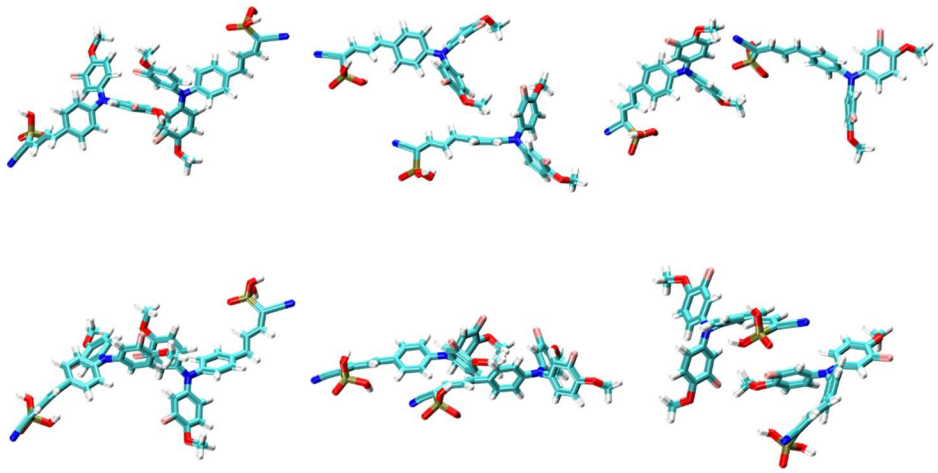

Supplementary Fig. 31 FTPA-CPA dimer packing conformation diagram observed in MD simulations.

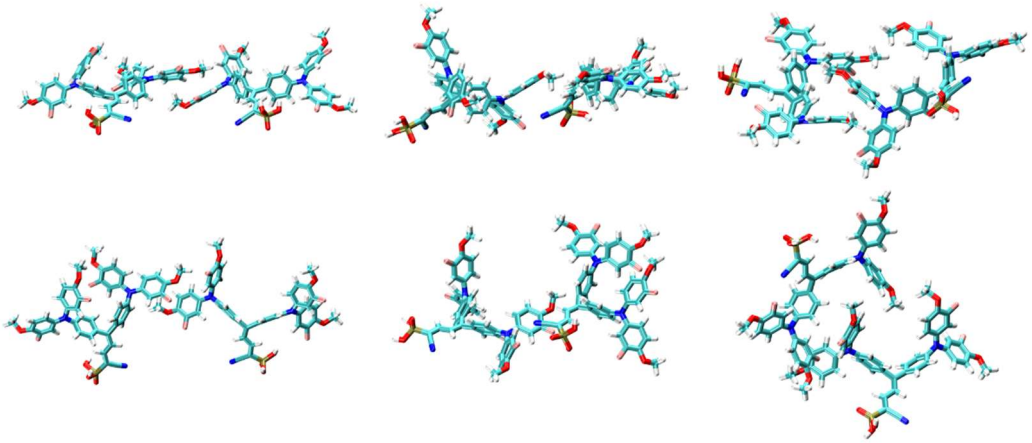

Supplementary Fig. 32 FMTPA-CPA dimer packing conformation diagram observed in MD simulations.

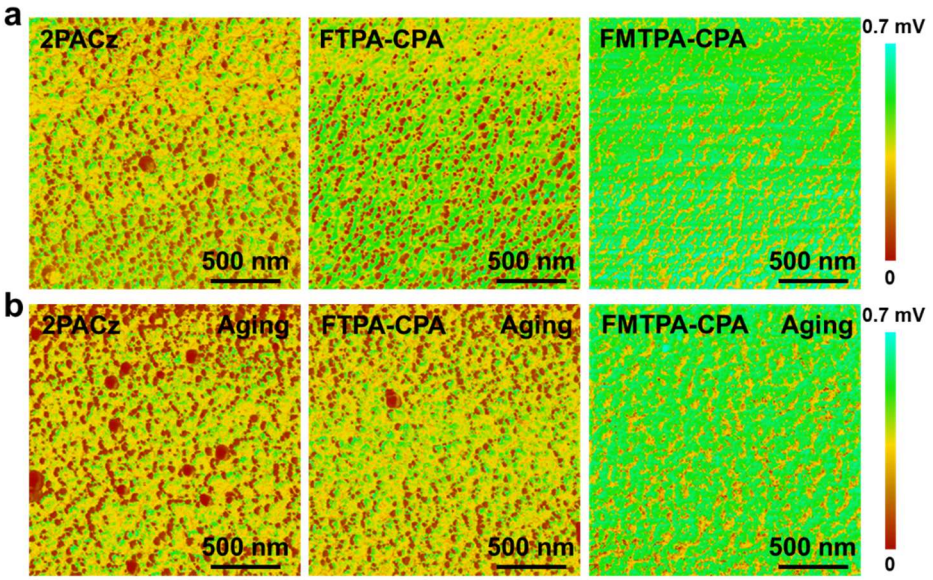

Supplementary Fig. 33 AFM-FTIR spectroscopy of 2PACz, FTPA-CPA and FMTPA-CPA on ITO substrate (a) before and (b) after aging under high temperature and illumination conditions.

Supplementary Fig. 34 Contact angels of the perovskite precursor solution on the 2PACz, FTPA-CPA and FMTPA-CPA SAMs.

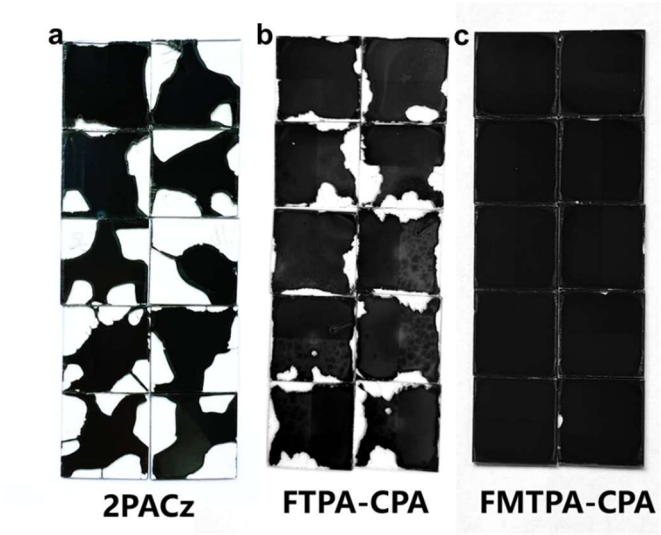

Supplementary Fig. 35 Photographs of perovskite films deposited on (a) 2PACz, (b) FTPA-CPA and (c) FMTPA-CPA SAMs.

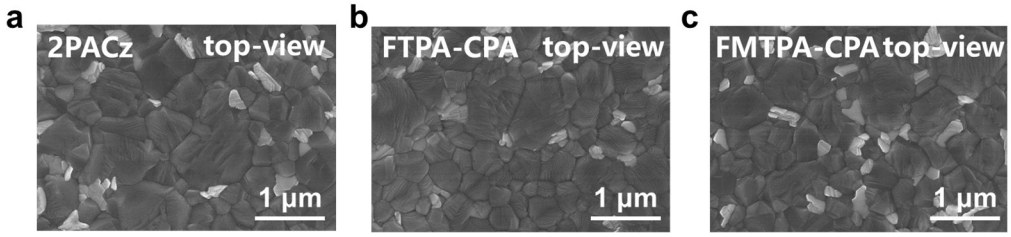

Supplementary Fig. 36 Top-view SEM images of perovskite films deposited on (a) 2PACz, (b) FTPA-CPA and (c) FMTPA-CPA SAMs. Scale bar: 1 μm.

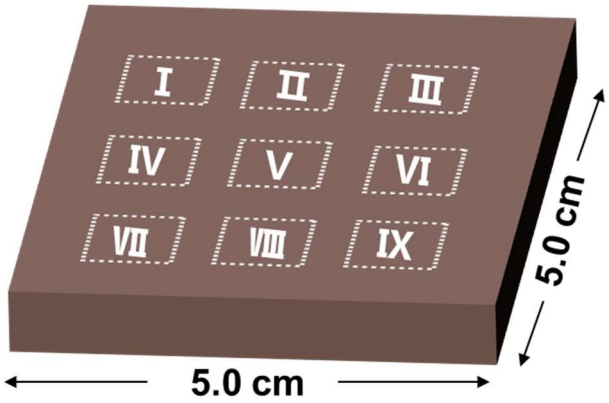

Supplementary Fig. 37 Schematic diagram of 9 platforms from 5.0 × 5.0 cm^2 perovskite films.

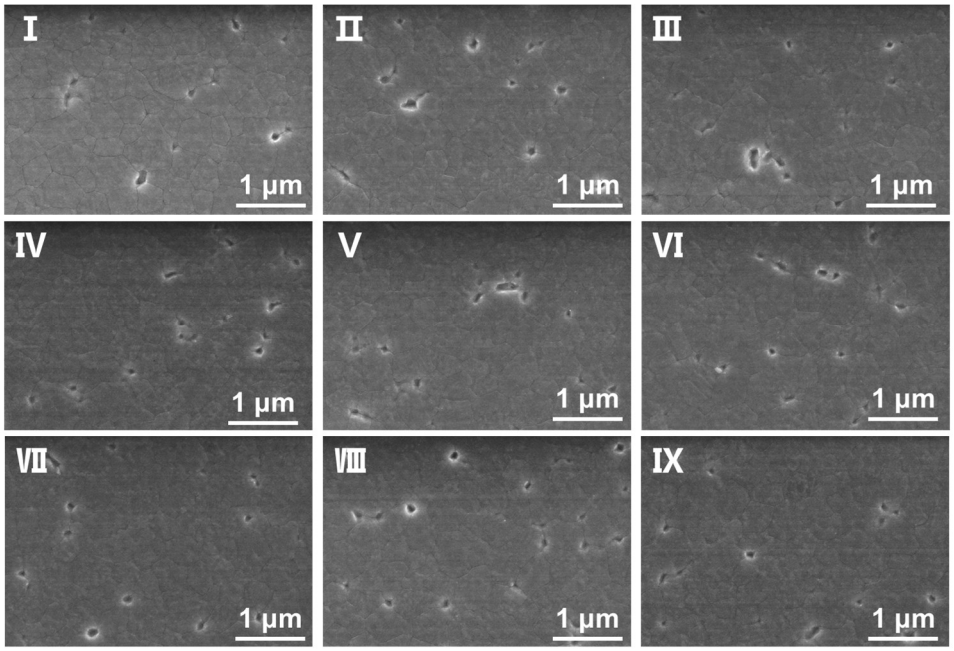

Supplementary Fig. 38 SEM images of the buried interface of 9 platforms in the large-area perovskite films deposited on 2PACz (5.0 × 5.0 cm^2). Scale bar: 1 μm.

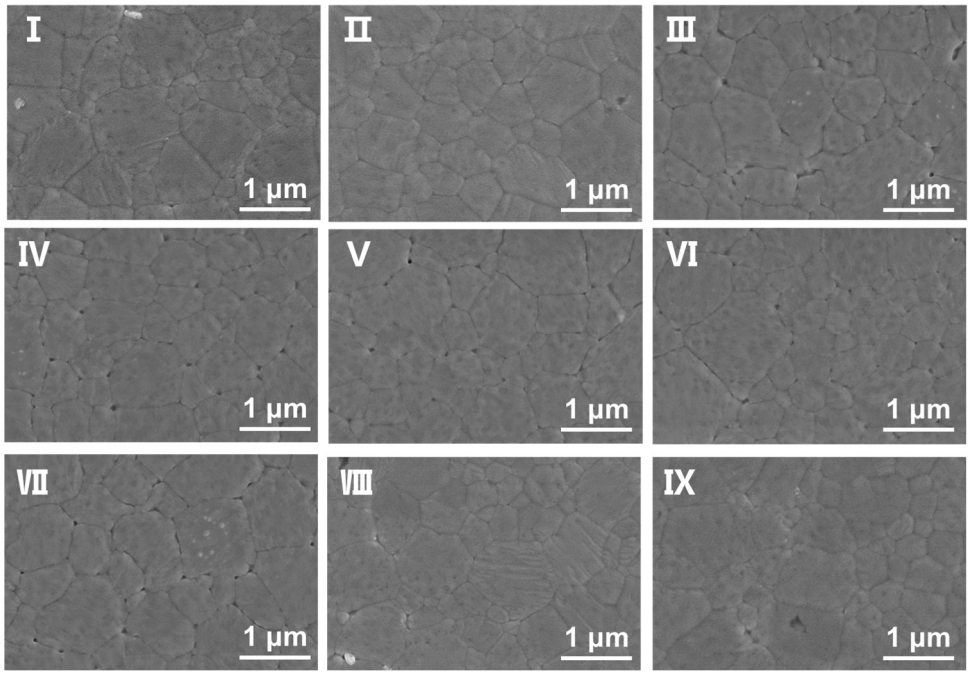

Supplementary Fig. 39 SEM images of the buried interface of 9 platforms in the large-area perovskite films deposited on FTPA-CPA (5.0 × 5.0 cm^2). Scale bar: 1 μm.

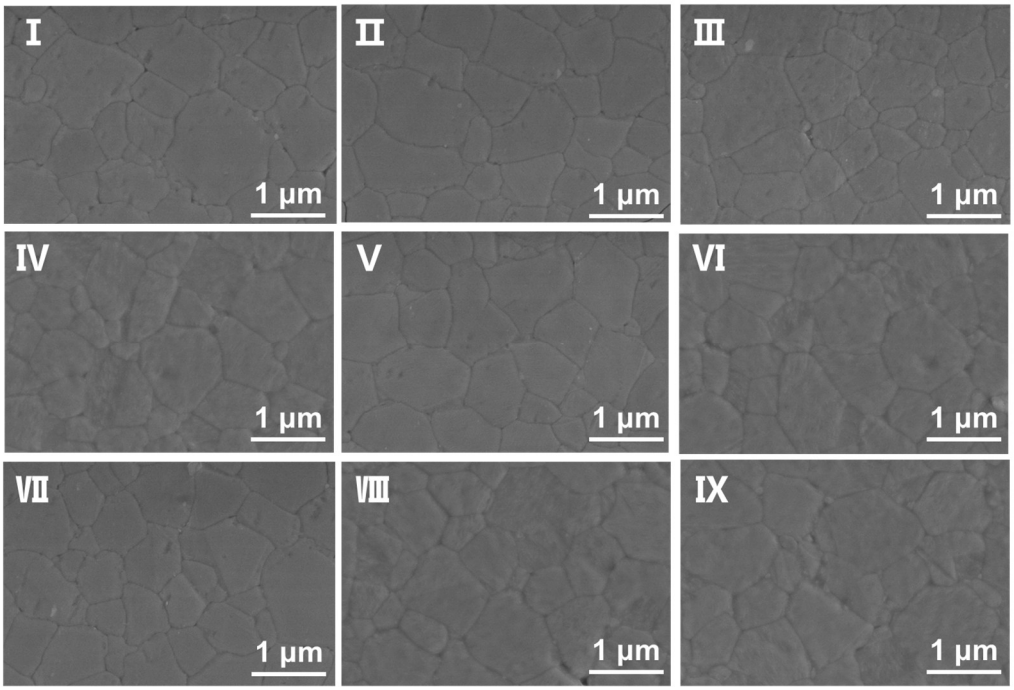

Supplementary Fig. 40 SEM images of the buried interface of 9 platforms in the large-area perovskite films deposited on FMTPA-CPA (5.0 × 5.0 cm^2). Scale bar: 1 μm.

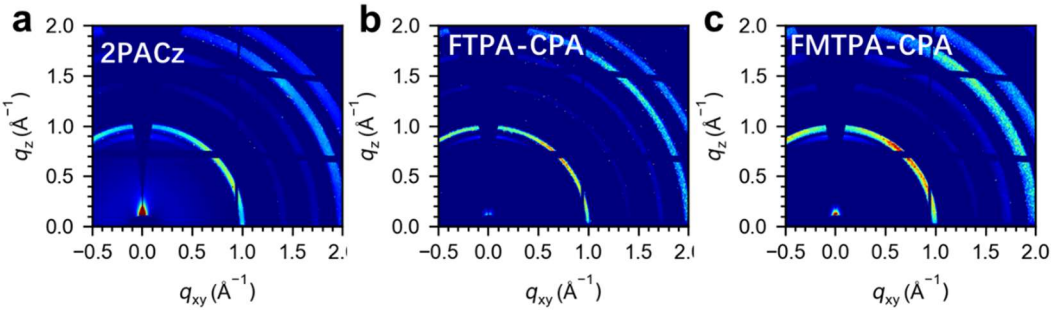

Supplementary Fig. 41 GIWAXS maps at grazing incidence angels of 0.5º of the buried interface of perovskite deposited on (a) 2PACz, (b) FTPA-CPA and (c) FMTPA-CPA SAMs.

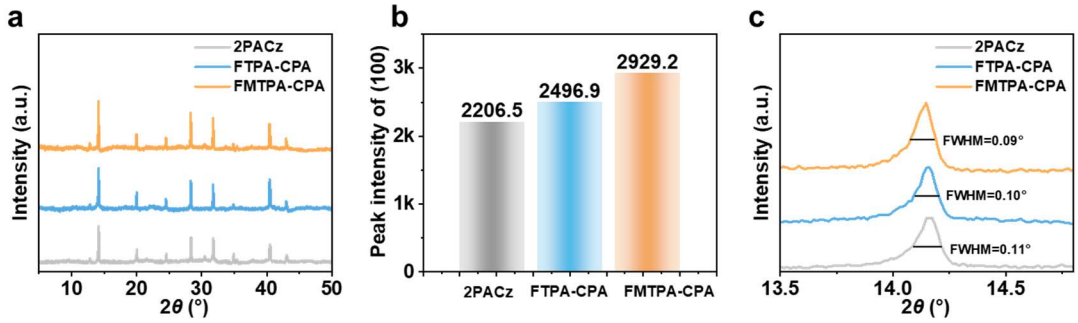

Supplementary Fig. 42 (a) XRD, (b) the intensity of (100) diffraction peak and (c) FWHM of (100) diffraction peak of the buried interface of perovskite deposited on 2PACz, FTPA-CPA and FMTPA-CPA SAMs.

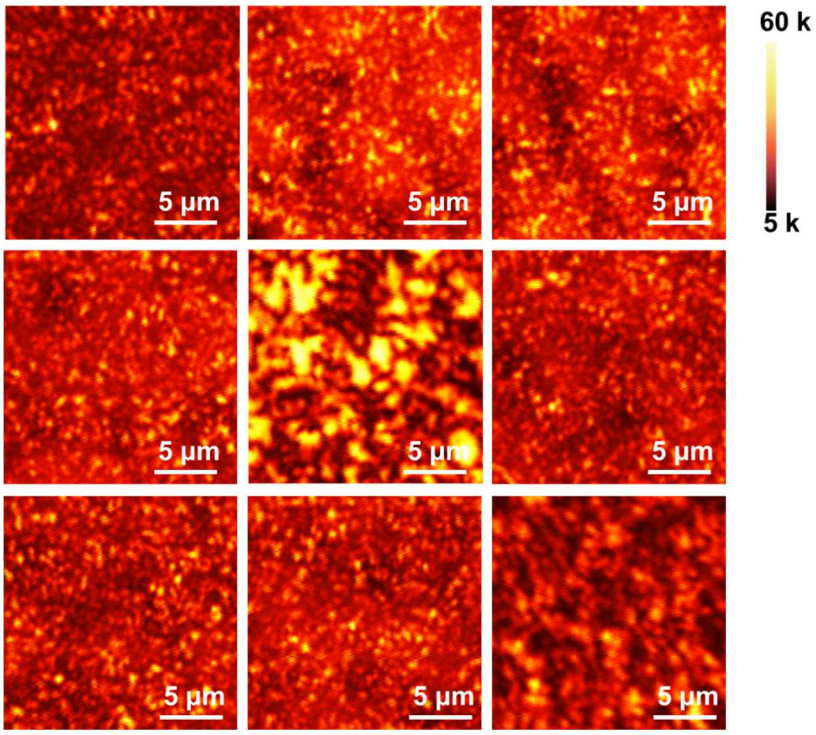

Supplementary Fig. 43 PL mapping of the buried interface of 9 platforms in the large-area perovskite films deposited on 2PACz (5.0 × 5.0 cm^2). Scale bar: 5 μm.

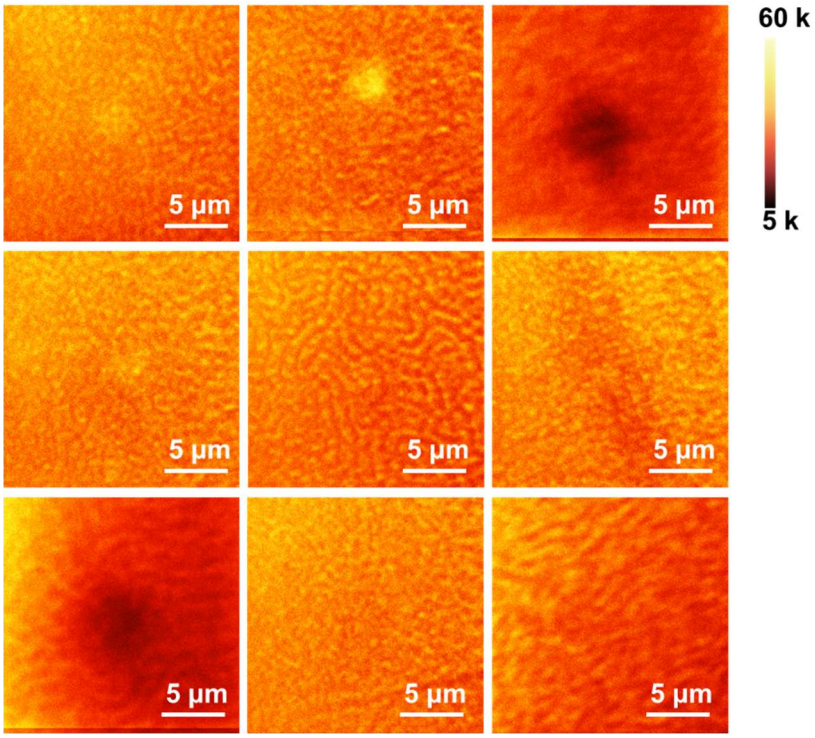

Supplementary Fig. 44 PL mapping of the buried interface of 9 platforms in the large-area perovskite films deposited on FTPA-CPA (5.0 × 5.0 cm^2). Scale bar: 5 μm.

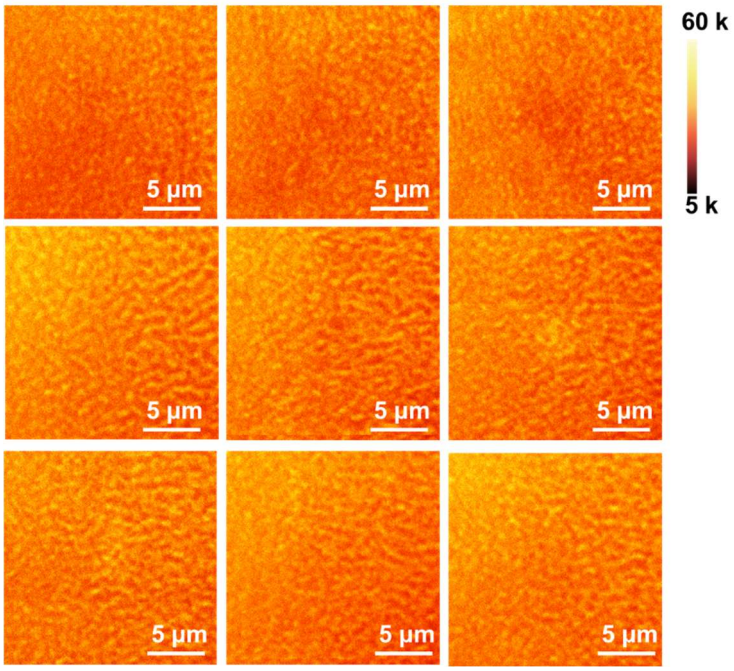

Supplementary Fig. 45 PL mapping of the buried interface of 9 platforms in the large-area perovskite films deposited on FMTPA-CPA (5.0 × 5.0 cm^2). Scale bar: 5 μm.

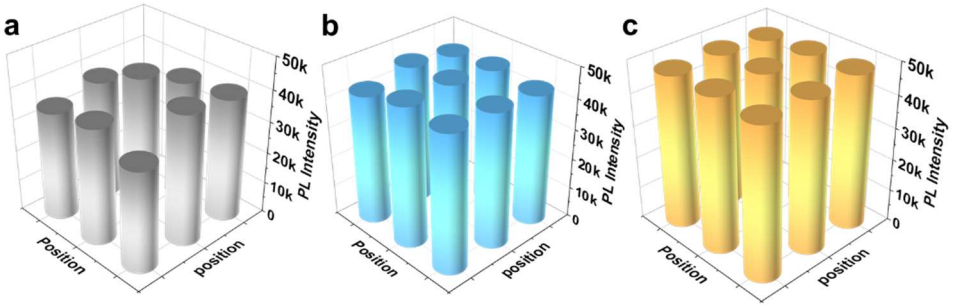

Supplementary Fig. 46 PL mapping corresponding intensities of the bottom surface of 9 platforms in the large-area perovskite films deposited on (a) 2PACz, (b) FTPA-CPA and (c) FMTPA-CPA (5.0 × 5.0 cm^2).

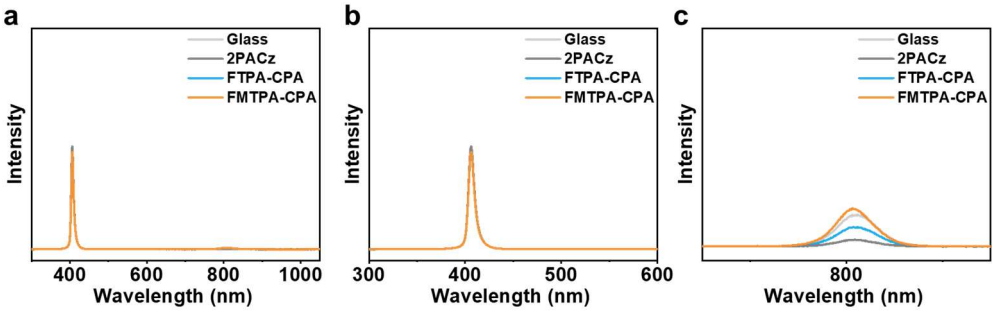

Supplementary Fig. 47 The complete PLQY spectra of perovskite films on (a) 2PACz, (b) FTPA-CPA and (c) FMTPA-CPA SAMs.

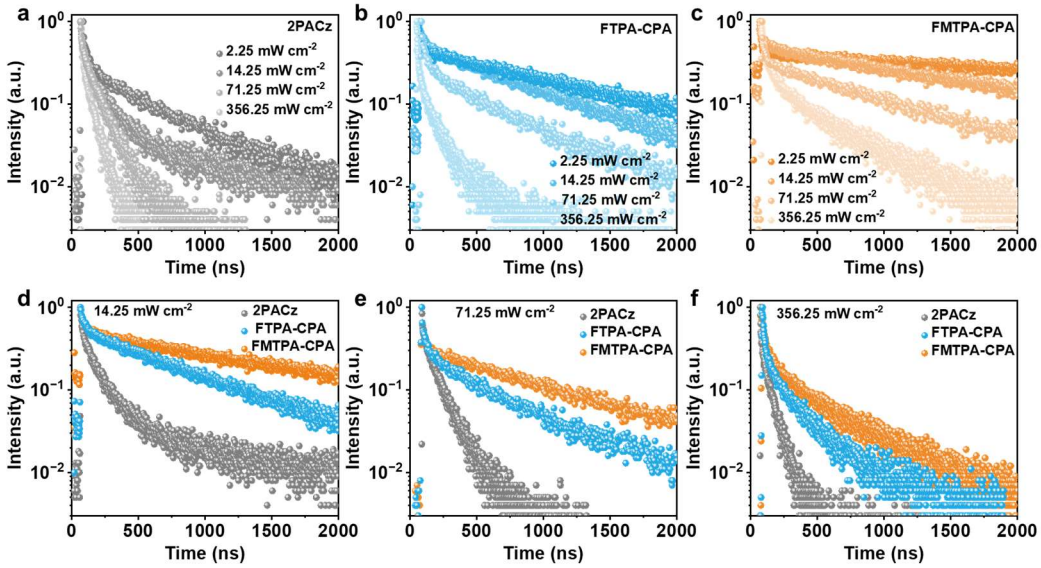

Supplementary Fig. 48 Excitation intensity-dependent photoluminescence decays of perovskite films on (a) 2PACz, (b) FTPA-CPA and (c) FMTPA-CPA SAMs using a 454 nm pulsed excitation. Comparison of the decay curves under identical excitation intensities of (d) 14.25 mW cm^{-2}, (e) 71.25 mW cm^{-2}, (f) 356.25 mW cm^{-2}.

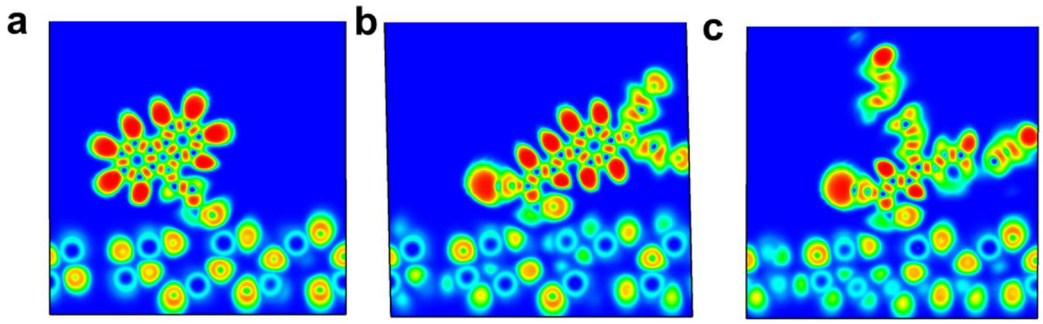

Supplementary Fig. 49 Electron Localization Function (ELF) in the SAM region on the ITO surface of (a) 2PACz, (b) FTPA-CPA and (c) FMTPA-CPA.

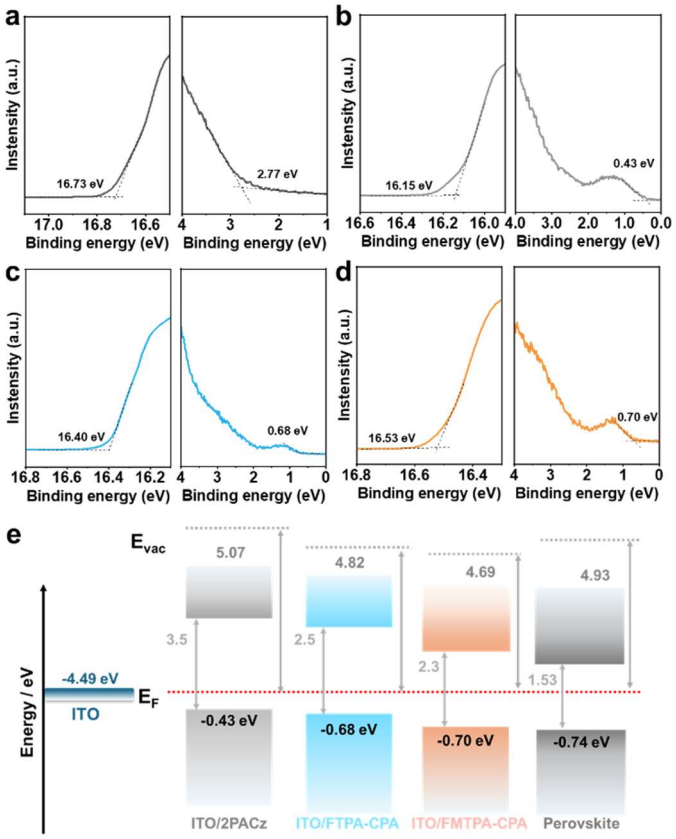

Supplementary Fig. 50 UPS cut-off edge of (a) Glass/ITO, (b) ITO/2PACz, (c) ITO/FTPA-CPA and (d) ITO/FMTPA-CPA; (e) Schematic illustration of energy level diagram (aligned with the Fermi-level).

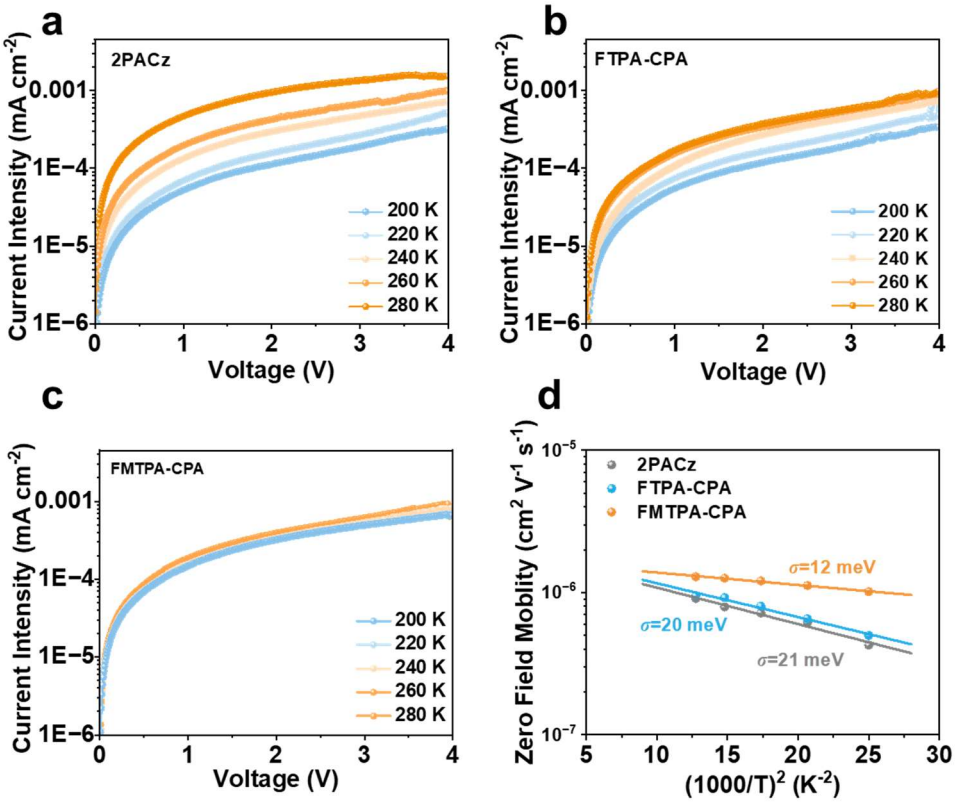

Supplementary Fig. 51 Temperature dependence of *J-V* curves for the hole-only devices based on the (a) 2PACz, (b) FTPA-CPA and (c) FMTPA-CPA films in dark. (d) Hole mobilities of the 2PACz, FTPA-CPA and FMTPA-CPA films as a function of $1/T^2$ were obtained using the equation for Gaussian disorder model (GDM).

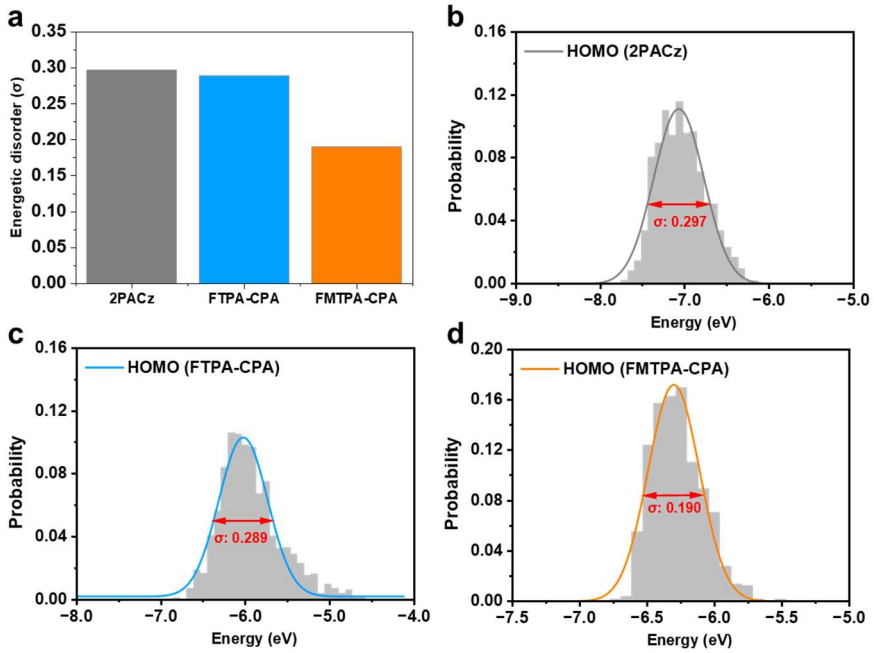

Supplementary Fig. 52 (a) The fitted energetic disorder values for 2PACz, FTPA-CPA and FMTPA-CPA by MD-DFT simulation; The probability distributions of HOMO energies, and the Gauss-fitted energetic disorder (σ) values for (b) 2PACz, (c) FTPA-CPA and (d) FMTPA-CPA by MD-DFT calculations.

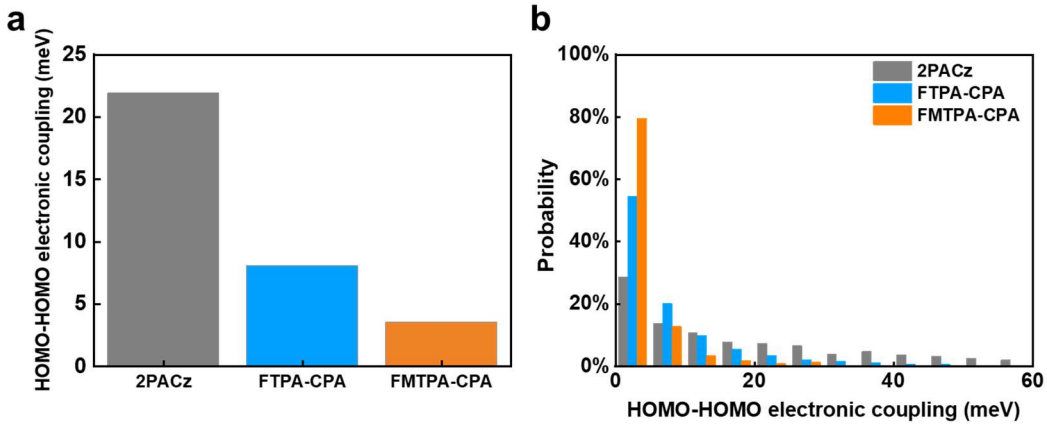

Supplementary Fig. 53 (a) Statistically averaged HOMO-HOMO electronic coupling values for dimers extracted from MD simulations and (b) probability distribution of HOMO-HOMO electronic coupling estimated by MD-DFT calculations for 2PACz, FTPA-CPA and FMTPA-CPA.

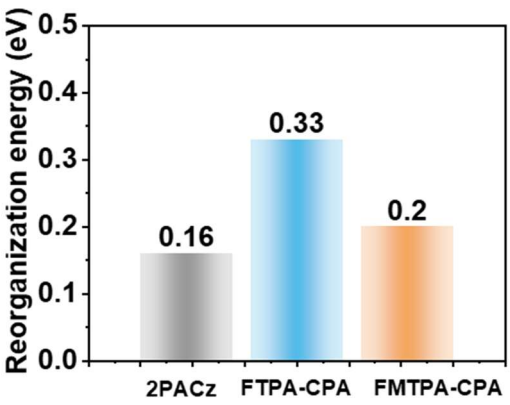

Supplementary Fig. 54 The reorganization energies of 2PACz, FTPA-CPA and FMTPA-CPA.

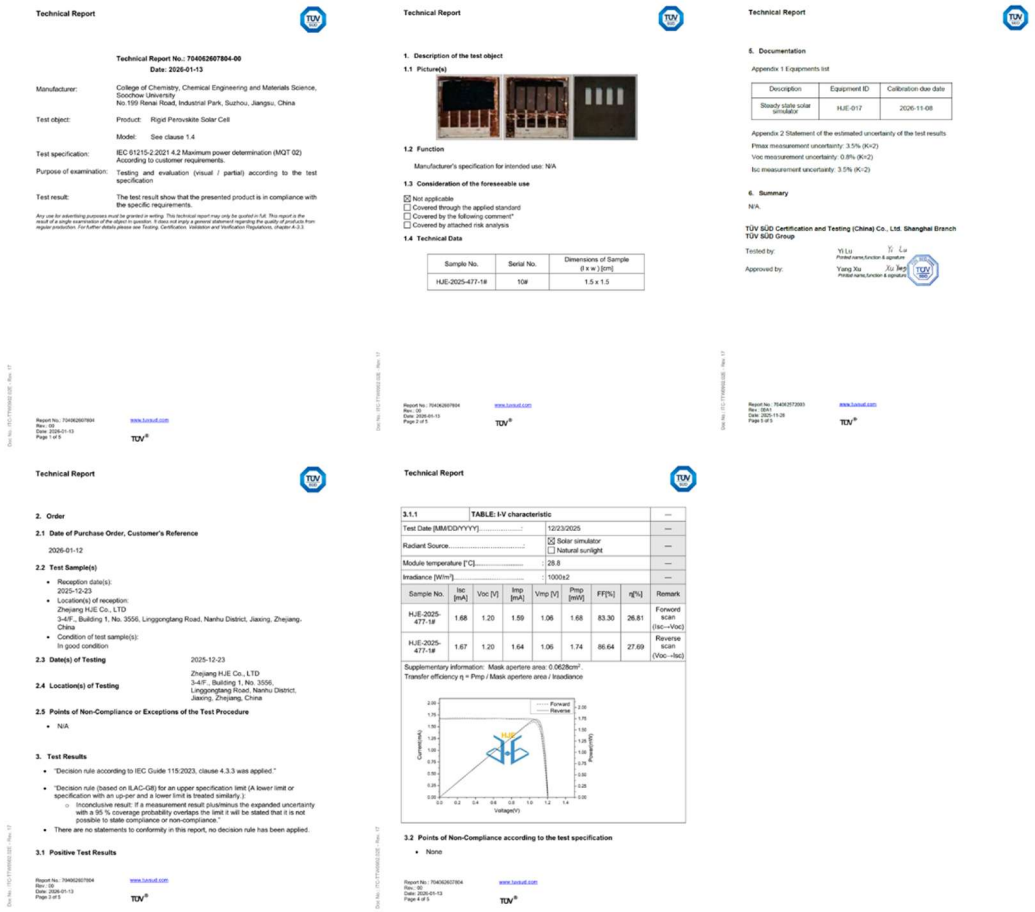

Supplementary Fig. 55 Certification report by TÜV SÜD for 0.063-cm^2 rigid pero-SC based on FMTPA-CPA.

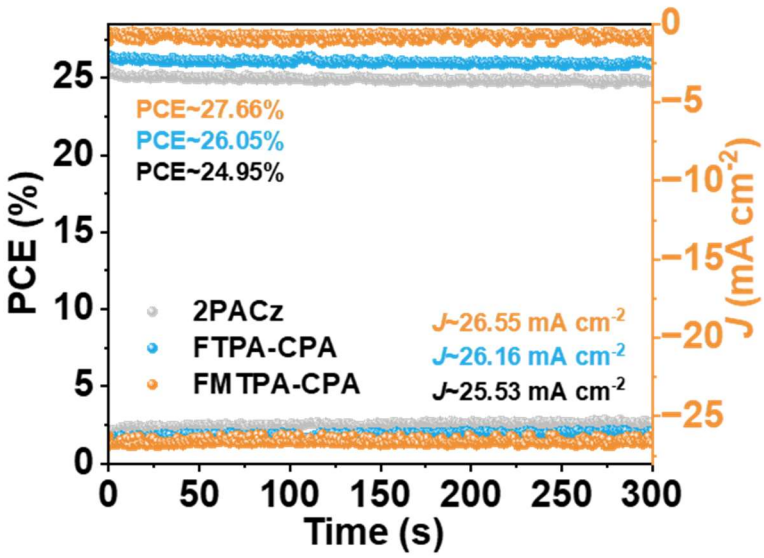

Supplementary Fig. 56 Maximal steady-state photocurrent output of the rigid small-area devices.

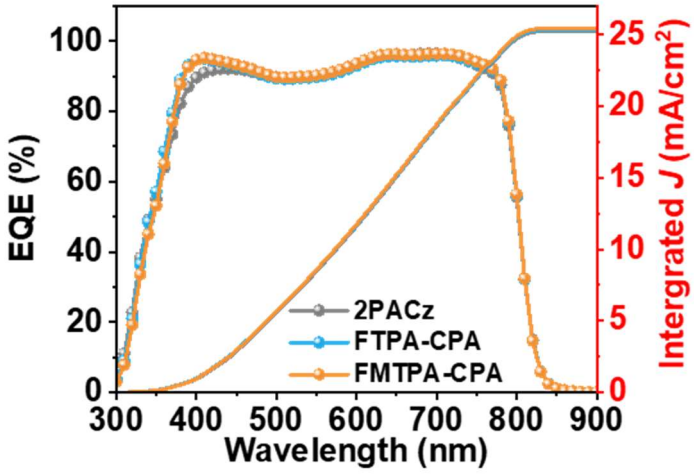

Supplementary Fig. 57 *EQE* spectra of pero-SCs based on 2PACz, FTPA-CPA and FMTPA-CPA.

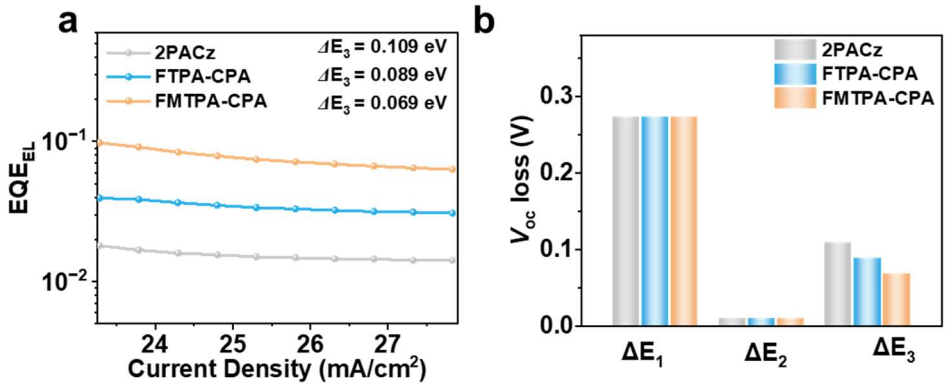

Supplementary Fig. 58 (a) EQE_{EL} and (b) energy losses of the devices based on 2PACz, FTPA-CPA and FMTPA-CPA SAMs.

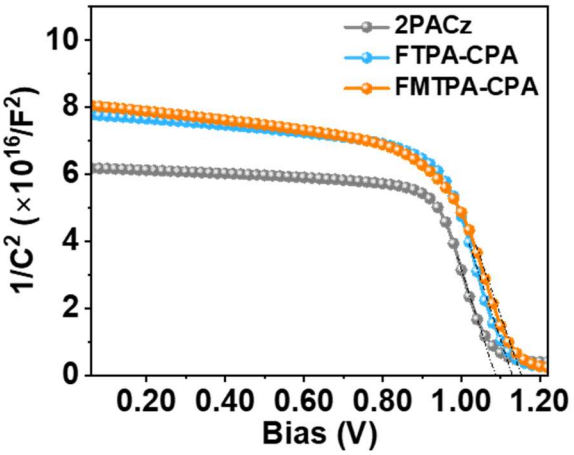

Supplementary Fig. 59 Mott-Schottky plots of the devices based on 2PACz, FTPA-CPA and FMTPA-CPA SAMs, obtained under dark conditions.

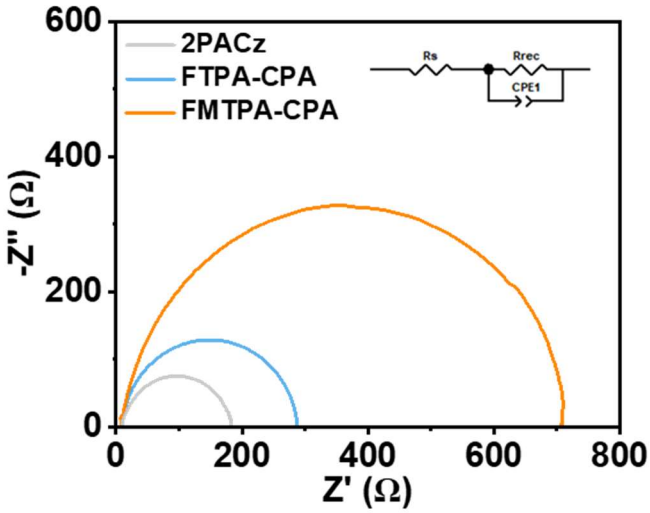

Supplementary Fig. 60 Nyquist plot of the pero-SCs based on 2PACz, FTPA-CPA and FMTPA-CPA SAMs under dark conditions (Inset shows the corresponding equivalent circuit).

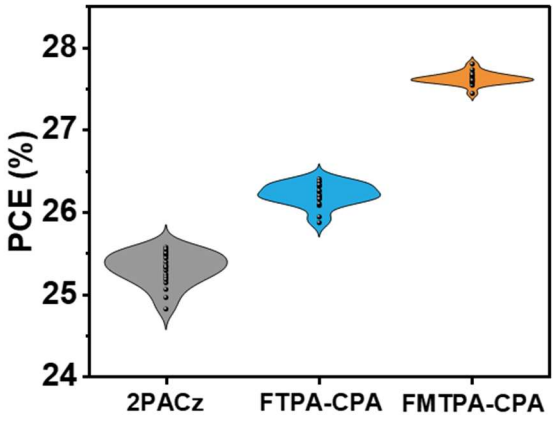

Supplementary Fig. 61 The statistics of PCE values obtained from *J-V* characteristic for devices based on 2PACz, FTPA-CPA and FMTPA-CPA SAMs (20 independent devices for each SAM).

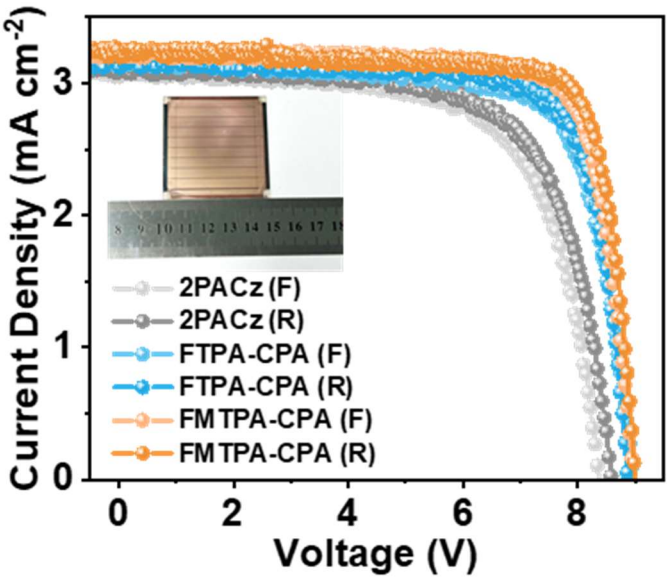

Supplementary Fig. 62 *J-V* curves of the champion large-area (15.64 cm^2) module based 2PACz, FTPA-CPA and FMTPA-CPA under AM1.5G 100 mW cm^{-2} illumination in the reverse and forward scan. Inset: a picture of the 5×5 cm^2 module.

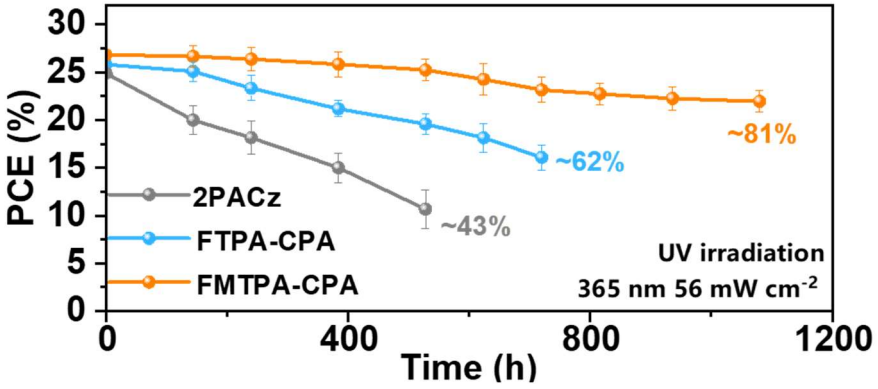

Supplementary Fig. 63 The UV irradiation stability at 365 nm (56 mW cm^{-2}) of small-area devices based on 2PACz, FTPA-CPA and FMTPA-CPA SAMs.

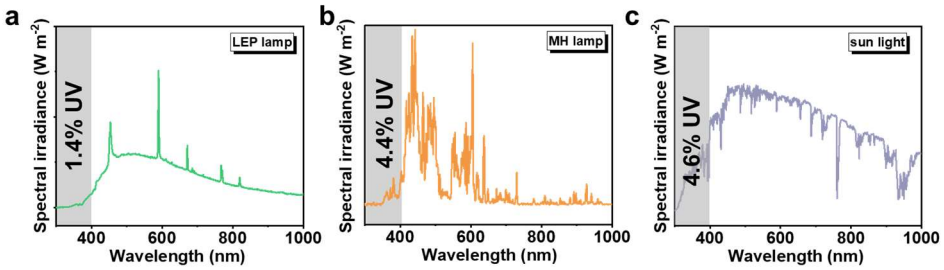

Supplementary Fig. 64 Spectrum of the light source for light-soaking stability tests (a) LEP lamp; (b) MH lamp and (c) sunlight. The inset showed the UV ratio of the lamp in each spectrum.

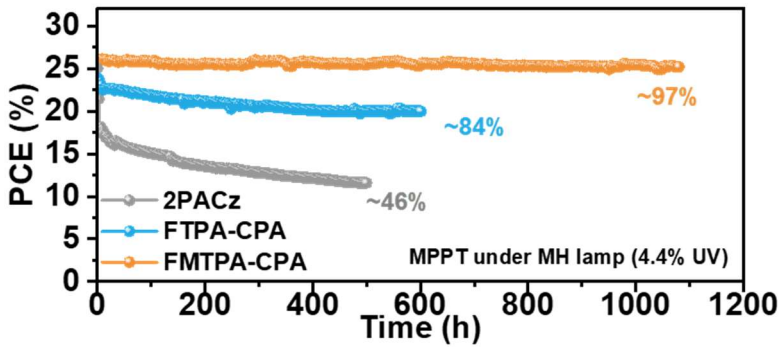

Supplementary Fig. 65 Light-soaking stability of small-area devices (MPPT conditions) based on 2PACz, FTPA-CPA and FMTPA-CPA under the illumination of MH lamp (100 mW cm^{-2}, 4.4% UV inside) in N_2 atmosphere.

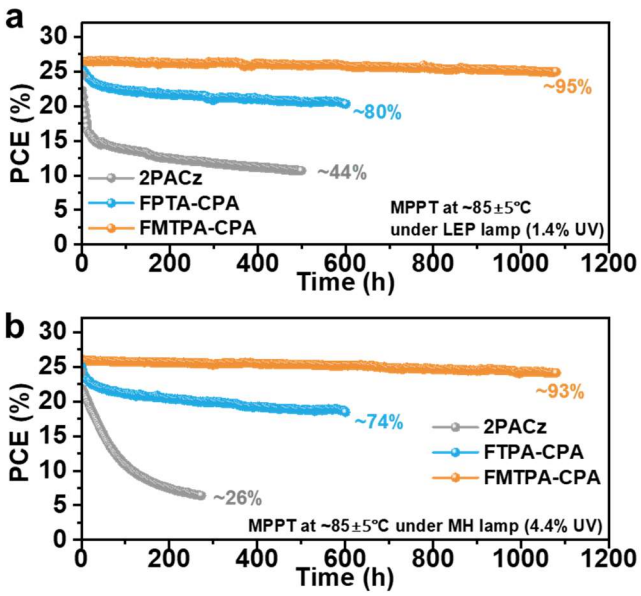

Supplementary Fig. 66 Light-soaking stability of small-area devices (MPPT conditions at 85±5 °C) based on 2PACz, FTPA-CPA and FMTPA-CPA under the illumination of (a) LEP lamp (100 mW cm^{-2}, 1.4% UV inside) and (b) MH lamp (100 mW cm^{-2}, 4.4% UV inside) at 85±5 °C in N_2 atmosphere.

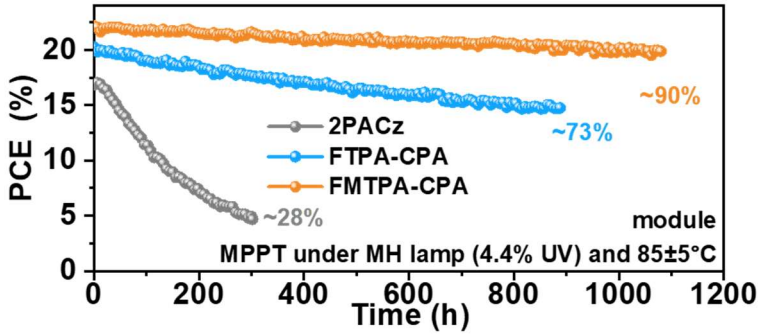

Supplementary Fig. 67 MPPT stability of modules based on 2PACz, FTPA-CPA and FMTPA-CPA at 85±5 °C under the illumination of MH lamp (100 mW cm^{-2}, 4.4% UV inside).

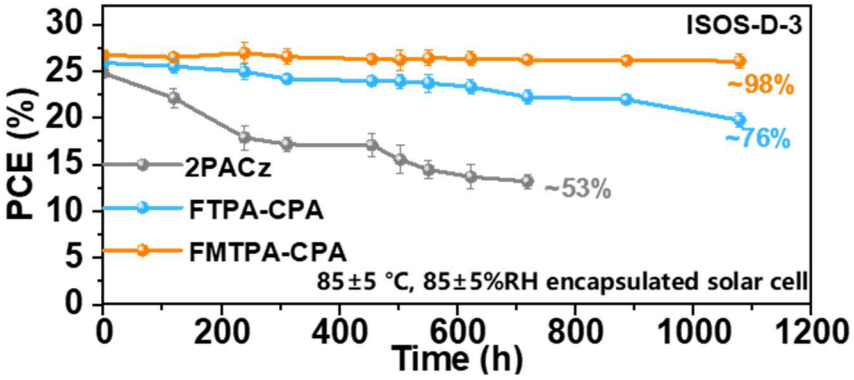

Supplementary Fig. 68 Stability of encapsulated devices aged under damp heat conditions (85±5 °C and 85±5% RH) following the ISOS-D-3 protocol.

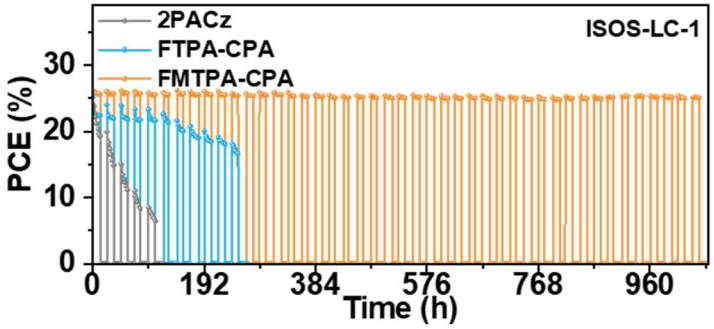

Supplementary Fig. 69 Stability of pero-SCs based on 2PACz, FTPA-CPA and FMTPA-CPA SAMs working in the day/night cycling modes following the ISOS-LC-1 protocol.

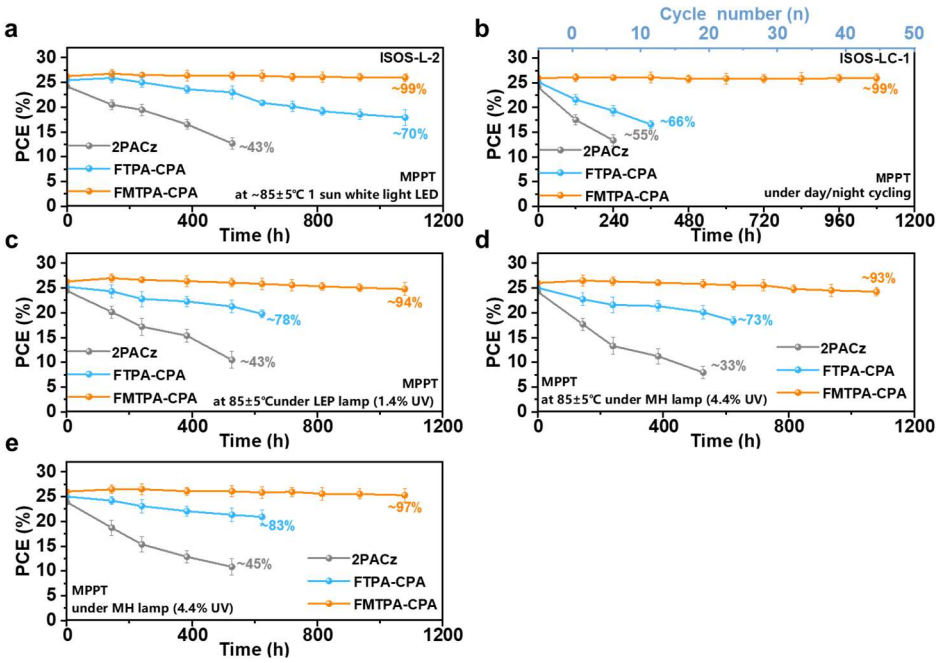

Supplementary Fig. 70 (a) Light-soaking stability of small-area devices under ISOS-L-2 protocol (MPPT conditions, 85±5 ℃, 10 independent devices); (b) Light-soaking stability of small-area devices under ISOS-LC-1 (MPPT conditions under day/night cycling, 10 independent devices); (c) Light-soaking stability of small-are devices (MPPT conditions under LEP lamp, 85±5 ℃, 10 independent devices); (d) Light-soaking stability of small-are devices (MPPT conditions under MH lamp, 85±5 ℃, 10 independent devices); (e) Light-soaking stability of small-are devices (MPPT conditions under MH lamp, 10 independent devices).

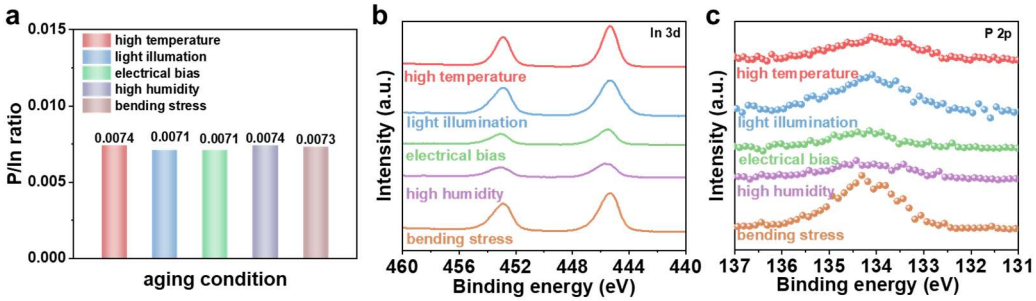

Supplementary Fig. 71 (a) The P/In ratio, (b) In 3d and (c) P 2p in XPS spectroscopy of 2PACz on ITO substrate before and after aging conditions, including high temperature (85±5 ℃ for 1000 h), light illumination (1 sun for 1000 h), electrical bias stressing (-2.0 V for 10 h), high humidity (85±5% RH for 1000 h), and bending stress (10000 cycles, 5 mm radius).

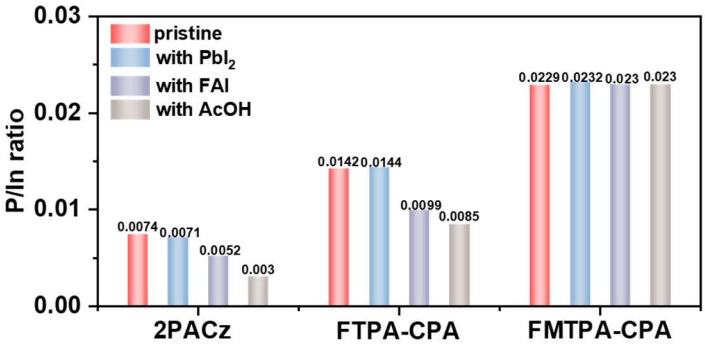

Supplementary Fig. 72 The P/In ratio of XPS spectroscopy of pristine 2PACz, FTPA-CPA and FMTPA-CPA on ITO substrate and with PbI_2 deposition, FAI deposition and AcOH soaking after aging under high temperature (85±5 ℃ for 1000 h).

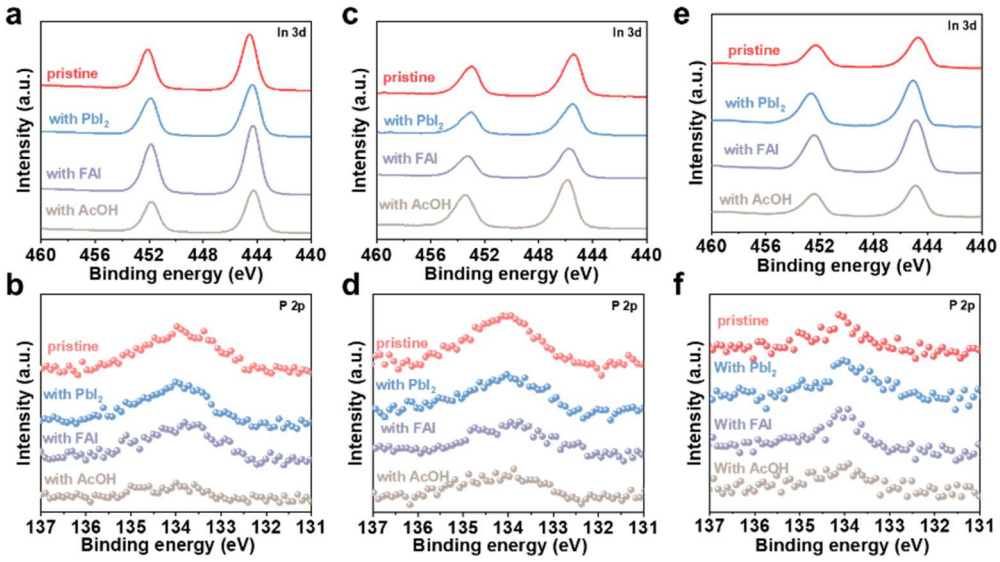

Supplementary Fig. 73 XPS spectra of (a) In 3d and (b) P 2p obtained from the pristine 2PACz and 2PACz with PbI_2 deposition, FAI deposition and AcOH soaking after aging under high temperature (85±5 ℃ for 1000 h). XPS spectra of (c) In 3d and (d) P 2p obtained from the pristine FTPA-CPA and FTPA-CPA with PbI_2 deposition, FAI deposition and AcOH soaking after aging under high temperature (85±5 ℃ for 1000 h). XPS spectra of (e) In 3d and (f) P 2p obtained from the pristine FMTPA-CPA and FMTPA-CPA with PbI_2 deposition, FAI deposition and AcOH soaking after aging under high temperature (85±5 ℃ for 1000 h).

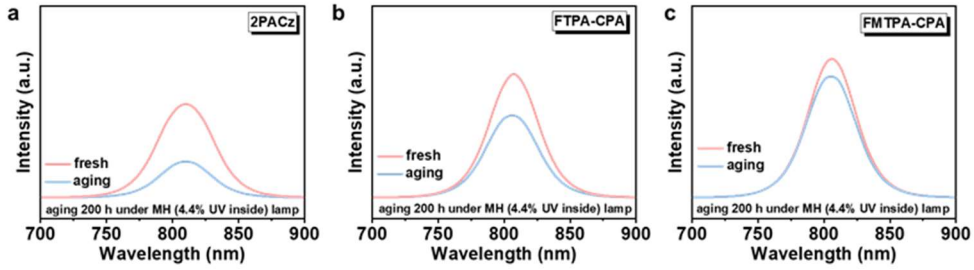

Supplementary Fig. 74 PL peak of buried perovskite interface based (a) 2PACz, (b) FTPA-CPA and (c) FMTPA-CPA before and after aging 200 h under the MH lamp.

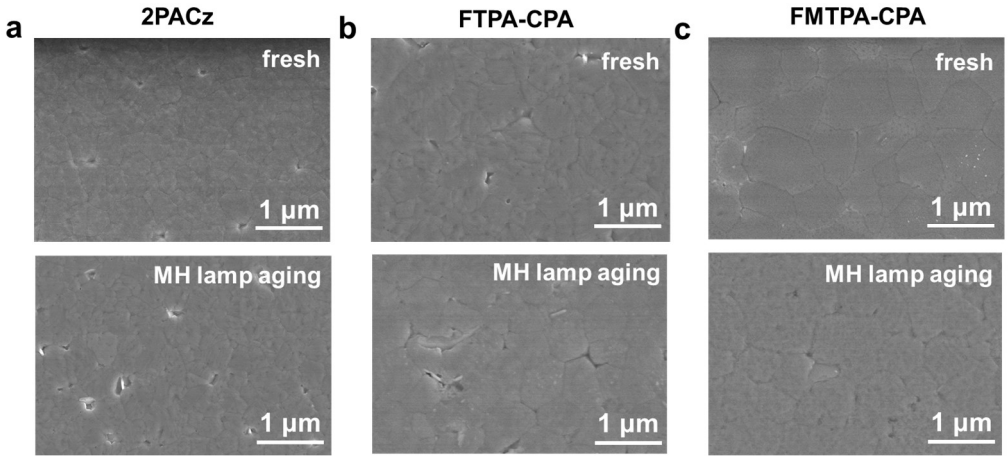

Supplementary Fig. 75 SEM of buried perovskite interface based (a) 2PACz, (b) FTPA-CPA and (c) FMTPA-CPA before and after aging 200 h under the MH lamp.

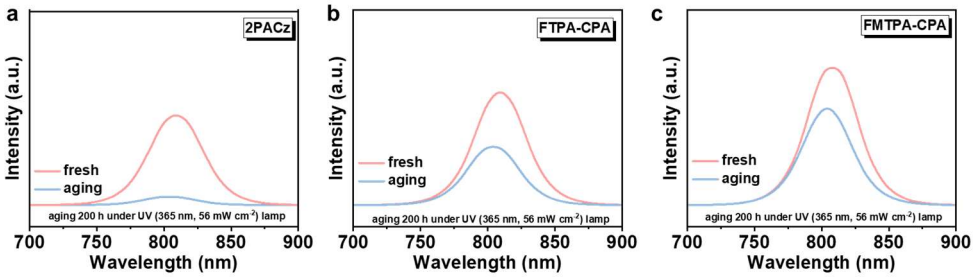

Supplementary Fig. 76 PL peak of buried perovskite interface based (a) 2PACz, (b) FTPA-CPA and (c) FMTPA-CPA before and after aging 200 h under the pure UV lamp (56 mW cm^{-2}).

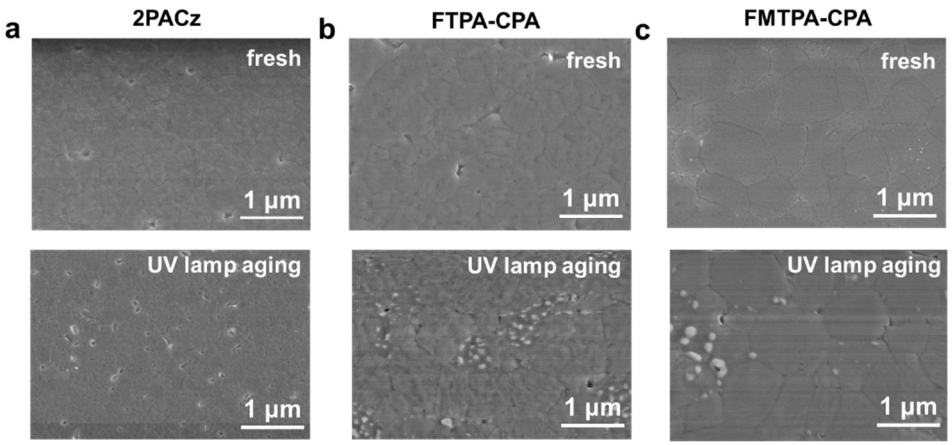

Supplementary Fig. 77 SEM of buried perovskite interface based (a) 2PACz, (b) FTPA-CPA and (c) FMTPA-CPA before and after aging 200 h under the pure UV lamp (56 mW cm^{-2}).

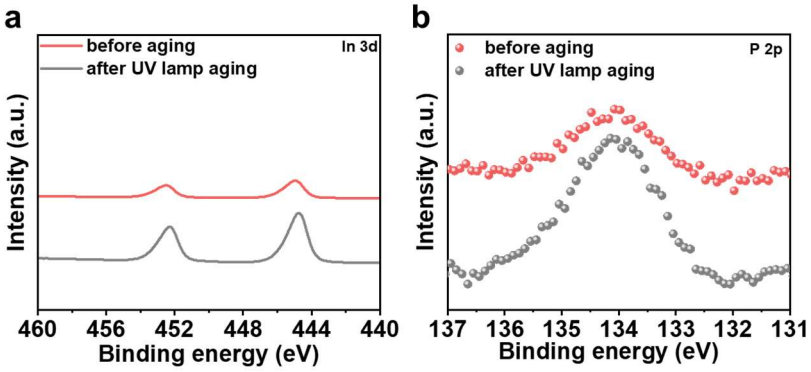

Supplementary Fig. 78 XPS spectra of (a)In 3d and (b) P 2p obtained from the FMTPA-CPA films before and after aging 200 h under pure UV lamp (56 mW cm^{-2}).

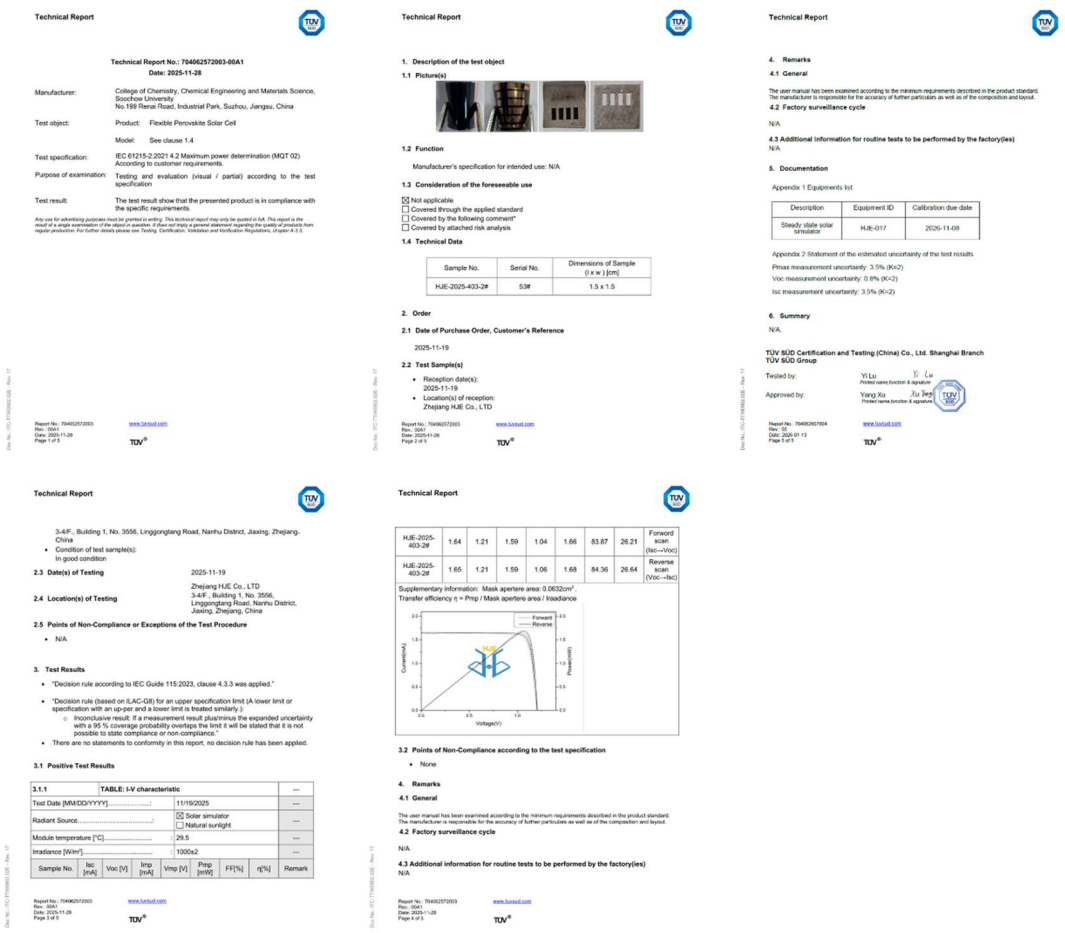

Technical Report

Technical Report No.: 704062572003-00A1
Date: 2025-11-28

Manufacturer: College of Chemistry, Chemical Engineering and Materials Science, Soochow University
No.199 Renai Road, Industrial Park, Suzhou, Jiangsu, China

Test object: Product: Flexible Perovskite Solar Cell
Model: See clause 1.4

Test specification: IEC 61215-2:2021 4.2 Maximum power determination (MQT 02) According to customer requirements.

Purpose of examination: Testing and evaluation (visual / partial) according to the test specification

Test result: The test result show that the presented product is in compliance with the specific requirements.

Any use for advertising purposes must be granted in writing. This technical report may only be quoted in full. This report is the result of a single examination of the object in question. It does not imply a general statement regarding the quality of products from regular production. For further details please see Testing, Certification, Validation and Verification Regulations, chapter 4.3.3.

1. Description of the test object

1.1 Picture(s)

1.2 Function

Manufacturer's specification for intended use: N/A

1.3 Consideration of the foreseeable use

☒ Not applicable
☐ Covered through the applied standard
☐ Covered by the following comment*
☐ Covered by attached risk analysis

1.4 Technical Data

Sample No.	Serial No.	Dimensions of Sample (l x w) [cm]
HJE-2025-403-2#	53#	1.5 x 1.5

2. Order

2.1 Date of Purchase Order, Customer's Reference

2025-11-19

2.2 Test Sample(s)

- Reception date(s):
  2025-11-19
- Location(s) of reception:
  Zhejiang HJE Co., LTD

4. Remarks

4.1 General

The user manual has been examined according to the minimum requirements described in the product standard. The manufacturer is responsible for the accuracy of further particulars as well as of the composition and layout.

4.2 Factory surveillance cycle

N/A

4.3 Additional information for routine tests to be performed by the factory(ies)

N/A

5. Documentation

Appendix 1 Equipments list

Description	Equipment ID	Calibration due date
Steady state solar simulator	HJE-017	2026-11-08

Appendix 2 Statement of the estimated uncertainty of the test results

Pmax measurement uncertainty: 3.5% (K=2)
Voc measurement uncertainty: 0.8% (K=2)
Isc measurement uncertainty: 3.5% (K=2)

6. Summary

N/A.

TÜV SÜD Certification and Testing (China) Co., Ltd. Shanghai Branch
TÜV SÜD Group

Tested by: Yi Lu
Approved by: Yang Xu

3-4/F., Building 1, No. 3556, Linggongtang Road, Nanhu District, Jiaxing, Zhejiang, China

- Condition of test sample(s):
  In good condition

2.3 Date(s) of Testing: 2025-11-19

2.4 Location(s) of Testing: Zhejiang HJE Co., LTD 3-4/F., Building 1, No. 3556, Linggongtang Road, Nanhu District, Jiaxing, Zhejiang, China

2.5 Points of Non-Compliance or Exceptions of the Test Procedure

- N/A

3. Test Results

- "Decision rule according to IEC Guide 115:2023, clause 4.3.3 was applied."
- "Decision rule (based on ILAC-G8) for an upper specification limit (A lower limit or specification with an up-per and a lower limit is treated similarly.):
  - Inconclusive result: If a measurement result plus/minus the expanded uncertainty with a 95 % coverage probability overlaps the limit it will be stated that it is not possible to state compliance or non-compliance."
- There are no statements to conformity in this report, no decision rule has been applied.

3.1 Positive Test Results

3.1.1	TABLE: I-V characteristic	—
Test Date [MM/DD/YYYY]	11/19/2025	—
Radiant Source	☒ Solar simulator ☐ Natural sunlight	—
Module temperature [°C]	29.5	—
Irradiance [W/m²]	1000±2	—

Sample No.	Isc [mA]	Voc [V]	Imp [mA]	Vmp [V]	Pmp [mW]	FF[%]	η[%]	Remark
HJE-2025-403-2#	1.64	1.21	1.59	1.04	1.66	83.87	26.21	Forword scan (Isc—Voc)
HJE-2025-403-2#	1.65	1.21	1.59	1.06	1.68	84.36	26.64	Reverse scan (Voc—Isc)

Supplementary information: Mask apertere area: 0.0632cm².
Transfer efficiency η = Pmp / Mask apertere area / Irradiance

3.2 Points of Non-Compliance according to the test specification

- None

4. Remarks

4.1 General

The user manual has been examined according to the minimum requirements described in the product standard. The manufacturer is responsible for the accuracy of further particulars as well as of the composition and layout.

4.2 Factory surveillance cycle

N/A

4.3 Additional information for routine tests to be performed by the factory(ies)

N/A

Supplementary Fig. 79 Certification report by TÜV SÜD for flexible small-area (0.063 cm^2) device based on FMTPA-CPA.

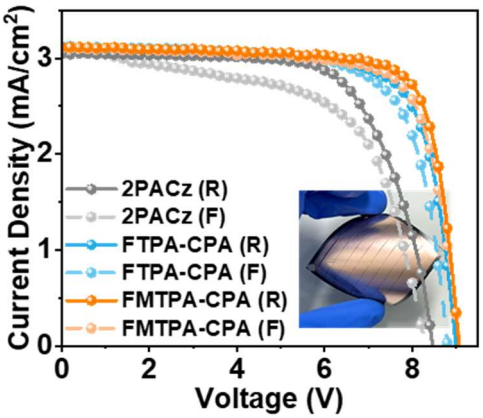

Supplementary Fig. 80 *J-V* curves of the champion flexible large-area (15.64 cm^2) modules based on FMTPA-CPA. Inset: a picture of the flexible 5×5 cm^2 module.

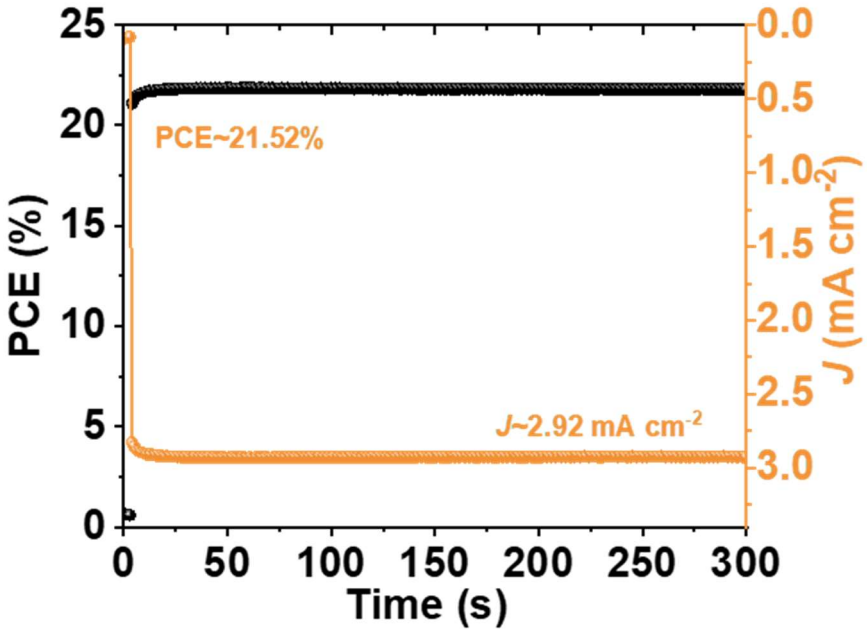

Supplementary Fig. 81 Maximal steady-state photocurrent output of the flexible large-area modules.

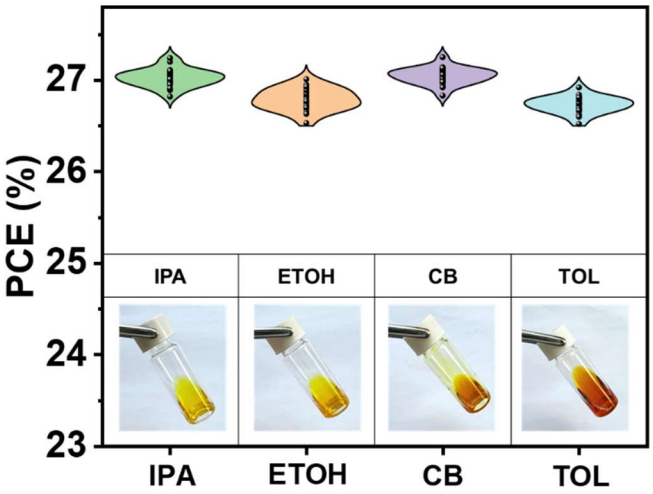

Supplementary Fig. 82 The statistics of PCE values obtained from *J-V* characteristic for devices based on different solvents, the inserted photographs are FMTPA-CPA SAMs in different solvents.

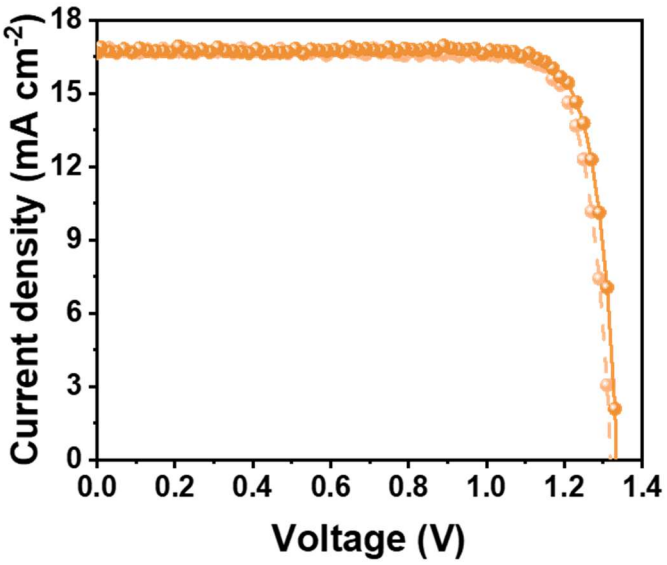

Supplementary Fig. 83 *J-V* curves of the 1.83 eV-bandgap pero-SCs based on FMTPA-CPA under AM 1.5G, 100 mW/cm^2 illumination.

Supplementary Tables

Supplementary Table 1 The element mass of FTPA-CPA and FMTPA-CPA.

Molecule	N (wt%)	C (wt%)	H (wt%)	CHN result	Molecular formula
FTPA-CPA	5.34	57.25	4.03	$NC_{12.51}H_{10.49}$	$N_2C_{25}H_{21}F_2O_5P$
FMTPA-CPA	5.60	71.98	4.83	$NC_{14.99}H_{11.99}$	$N_3C_{45}H_{36}F_4O_7P$

Supplementary Table 2 The N_{FOD} values of 2PACz, FTPA-CPA and FMTPA-CPA.

Molecule	2PACz	FTPA-CPA	FMTPA-CPA
N_{FOD}	0.10	0.43	0.66

Supplementary Table 3 Quantitative ESR data of 2PACz, FTPA-CPA and FMTPA-CPA sample.

Samples	amount of substance (mol)	Integrated peaks area	Ratio of free radicals/samples
2PACz	1.45×10^{-5}	6.55	2.20×10^{-5}
FTPA-CPA	1.28×10^{-5}	33.30	1.27×10^{-4}
FMTPA-CPA	1.20×10^{-5}	216.63	8.86×10^{-3}
TEMPO	1.94×10^{-9}	39.74	1

Supplementary Table 4 Crystallographic data of FMTPA.

Compound	FMTPA
CCDC no.	2442679
Empirical formula	$C_{42}H_{34}F_4N_2O_4$
Formula weight	706.71
Temperature/K	223
Crystal system	monoclinic
Space group	$P2_1/c$
a/Å	17.208(3)
b/Å	7.1330(12)
c/Å	29.674(5)
α/°	90
β/°	98.668(5)
γ/°	90
Volume/Å^3	3600.7(11)
Z	4
ρ_{calc}g/cm^3	1.304
μ/mm^{-1}	0.098
F(000)	1472.0
Crystal size/mm^3	0.3 × 0.2 × 0.1
Radiation	MoKα (λ = 0.71073)
2Θ range for data collection/°	3.93 to 50.054
Index ranges	$-20 \le h \le 20$, $-8 \le k \le 8$, $-35 \le l \le 35$
Reflections collected	56462
Independent reflections	6132 [R_{int} = 0.0899, R_{sigma} = 0.0469]
Data/restraints/parameters	6132/9/474
Goodness-of-fit on F^2	1.145
Final R indexes [I>=2σ (I)]	R_1 = 0.1102, wR_2 = 0.3247
Final R indexes [all data]	R_1 = 0.1334, wR_2 = 0.3425
Largest diff. peak/hole / e Å^{-3}	1.00/-0.57

Supplementary Table 5 The electrostatic potential of oxygen atoms within phosphonic acid groups from ESP calculation.

SAMs	-P=O (kcal/mol)	-P-OH(1) (kcal/mol)	-P-OH(2) (kcal/mol)
2PACz	–23.50	–6.45	–6.46
FTPA-CPA	–28.20	–18.88	–14.61
FMTPA-CPA	–31.11	–20.72	–15.61

Supplementary Table 6 DFT simulations of the acid dissociation constant of phosphonic acid group in different solvents on the 2PACz, FTPA-CPA and FMTPA-CPA.

SAMs	solvent	pKa_1
2PACz	H_2O	8.26
	EtOH	12.84
FTPA-CPA	H_2O	5.34
	EtOH	9.59
FMTPA-CPA	H_2O	1.66
	EtOH	5.80
H_3PO_4	H_2O	1.23
	EtOH	5.96

Supplementary Table 7 XPS spectra analysis obtained from the 2PACz, FTPA-CPA and FMTPA-CPA films.

SAM	condition	In area	P area	P/In
2PACz	fresh	343184.6	3809.4	0.0111
	EtOH washing	481605.7	3525.1	0.0073
	EtOH soaking	949840.9	5760.1	0.0061
	H_3BO_3 washing	745977.2	4105.9	0.0055
	AcOH washing	1124496.7	4625.0	0.0041
	aging (1 sun & 85 ℃)	691893.6	4013.0	0.0058
FTPA-CPA	fresh	340987.6	5591.7	0.0164
	EtOH washing	372394.9	5245.5	0.0141
	EtOH soaking	338204.6	4531.3	0.0134
	H_3BO_3 washing	674946.0	6117.5	0.0091
	AcOH washing	798210.7	5438.9	0.0068
	aging (1 sun & 85 ℃)	422132.5	4945.0	0.0117
FMTPA-CPA	fresh	212335.0	5482.0	0.0258
	EtOH washing	183058.1	4228.6	0.0231
	EtOH soaking	258752.7	5908.2	0.0228
	H_3BO_3 washing	237409.8	5515.6	0.0232
	AcOH washing	229678.7	5339.9	0.0233
	aging (1 sun & 85 ℃)	279105.3	6284.6	0.0225
	aging under UV lamp	536154.2	12281.1	0.0229

Supplementary Table 8 The surface coverage rate in MD simulations.

SAMs	coverage
2PACz	50.2%
FTPA-CPA	62.3%
FMTPA-CPA	66.3%

Supplementary Table 9 Binding energy of SAM dimers.

SAMs	Bind energy (kJ/mol)
2PACz	–61.9
FTPA-CPA	–39.9
FMTPA-CPA	–40.0

Supplementary Table 10 TRPL decay fitting parameters of perovskite deposited on 2PACz, FTPA-CPA and FMTPA-CPA SAMs under excitation intensities of 14.25 mW cm^{-2}.

SAMs	τ_1 (ns)	f_1 (%)	τ_2 (ns)	f_2 (%)	τ_{avg} (ns)
2PACz	24.709	25.625	73.496	74.496	68.439
FTPA-CPA	31.139	4.001	688.884	95.999	687.647
FMTPA-CPA	33.375	2.204	1171.241	97.796	1170.575

Supplementary Table 11 Photovoltaic parameters of pero-SCs under AM1.5G, 100 mW/cm^2 illumination. Forward scan: –0.2 V→1.2 V (small-area), –0.5 V→9.5 V (module); Reverse scan: 1.2 V→–0.2 V (small-area), 9.5 V→–0.5 V (module).

Substrate type	SAMs	Scan direction	V_{oc} (V)	J_{sc} (mA/cm^2)	FF (%)	PCE_{max}[a](PCE_{avg})[a] (%)
Glass/ITO (0.063 cm^2)	2PACz	Reverse	1.18 (1.17±0.02)	26.46 (26.50±0.15)	81.9 (81.9±1.8)	25.57 (25.30±0.20)
		Forward	1.18 (1.16±0.02)	26.47 (26.48±0.13)	79.3 (79.0±1.7)	24.77 (24.35±0.30)
	FTPA-CPA	Reverse	1.19 (1.20±0.02)	26.44 (26.53±0.12)	83.9 (82.6±1.4)	26.40 (26.21±0.14)
		Forward	1.19 (1.19±0.01)	26.57 (26.49±0.13)	79.5 (79.2±1.1)	25.14 (24.91±0.19)
	FMTPA-CPA	Reverse	1.20 (1.20±0.01)	26.59 (26.52±0.10)	86.6 (86.5±0.2)	27.69 (27.62±0.07)
		Forward	1.20 (1.20±0.01)	26.75 (26.65±0.11)	83.3 (82.9±0.5)	26.81 (26.65±0.09)
Glass/ITO (15.64 cm^2)	2PACz	Reverse	8.58 (8.46±0.19)	3.11 (3.10±0.02)	69.3 (69.3±1.0)	18.49 (18.17±0.22)
		Forward	8.37 (8.28±0.15)	3.10 (3.10±0.01)	68.5 (68.0±1.3)	17.77 (17.46±0.21)
	FTPA-CPA	Reverse	8.88 (8.83±0.09)	3.19 (3.18±0.01)	77.0 (76.8±1.0)	21.81 (21.54±0.19)
		Forward	8.87 (8.79±0.09)	3.20 (3.20±0.02)	74.5 (74.3±0.8)	21.15 (20.92±0.16)
	FMTPA-CPA	Reverse	9.00 (9.01±0.08)	3.25 (3.24±0.02)	80.8 (80.6±0.8)	23.63 (23.48±0.08)
		Forward	8.96 (8.94±0.09)	3.24 (3.23±0.02)	79.1 (78.9±0.8)	22.96 (22.80±0.06)
PET/ITO (0.063 cm^2)	2PACz	Reverse	1.17 (1.17±0.02)	25.62 (25.64±0.07)	81.2 (80.3±0.9)	24.35 (23.88±0.22)
		Forward	1.17 (1.16±0.01)	25.04 (25.18±0.07)	79.7 (78.6±0.9)	23.35 (22.95±0.19)

Substrate type	SAMs	Scan direction	V_{oc} (V)	J_{sc} (mA/cm^2)	FF (%)	PCE_{max}[a](PCE_{avg})[a] (%)
PET/ITO (0.063 cm^2)	FTPA-CPA	Reverse	1.19 (1.19±0.01)	25.81 (25.85±0.05)	83.3 (81.9±0.7)	25.58 (25.09±0.20)
		Forward	1.18 (1.17±0.01)	25.88 (25.88±0.08)	80.0 (79.8±0.5)	24.42 (24.25±0.10)
	FMTPA-CPA	Reverse	1.21 (1.20±0.01)	26.17 (26.19±0.09)	84.4 (84.2±0.9)	26.64 (26.45±0.13)
		Forward	1.21 (1.20±0.01)	25.88 (26.04±0.08)	83.9 (83.5±0.7)	26.21 (26.03±0.11)
PET/ITO (15.64 cm^2)	2PACz	Reverse	8.46 (8.23±0.10)	3.11 (3.12±0.01)	64.8 (64.0±0.5)	17.06 (16.48±0.16)
		Forward	8.30 (8.02±0.12)	3.07 (3.10±0.01)	61.4 (61.1±0.5)	15.63 (15.22±0.14)
	FTPA-CPA	Reverse	8.98 (8.78±0.09)	3.14 (3.13±0.01)	74.7 (75.0±0.6)	21.07 (20.64±0.14)
		Forward	8.80 (8.65±0.11)	3.13 (3.13±0.01)	72.9 (72.8±0.8)	20.08 (19.69±0.13)
	FMTPA-CPA	Reverse	9.07 (9.08±0.06)	3.14 (3.14±0.01)	77.9 (77.5±0.5)	22.18 (22.12±0.06)
		Forward	9.07 (9.05±0.07)	3.14 (3.14±0.01)	75.4 (75.3±0.5)	21.46 (21.41±0.05)

[a] The maximum PCE, average PCE, and standard deviations of 20 devices.

Supplementary Table 12 Statistical energy losses of the devices based on 2PACz, FTPA-CPA and FMTPA-CPA.

SAMs	E_g (eV)	ΔE_1(eV)	ΔE_2 (eV)	ΔE_3 (eV)
2PACz	1.53	0.27	0.010	0.109
FTPA-CPA	1.53	0.27	0.010	0.089
FMTPA-CPA	1.53	0.27	0.010	0.069

Supplementary Table 13 Resistance and capacitance values of the pero-SCs based on 2PACz, FTPA-CPA and FMTPA-CPA SAMs under dark conditions.

SAMs	Rs (Ω)	Rp (Ω)	C (nF)
2PACz	8.841	275.4	12.359
FTPA-CPA	10.95	165.8	12.791
FMTPA-CPA	9.477	677.8	8.157

Supplementary Table 14 Photovoltaic parameters of 20 independent pero-SCs based on FMTPA-CPA under AM1.5G, 100 mW/cm^2 illumination. Forward scan: –0.2 V→1.2 V; Reverse scan: 1.2 V→ –0.2 V.

	V_{oc} (V)	J_{sc} (mA/cm^2)	FF (%)	PCE_{max}[a](PCE_{avg})[a] (%)
1#	1.20	26.59	86.64	27.69
2#	1.20	26.61	86.33	27.57
3#	1.20	26.58	86.34	27.54
4#	1.21	26.35	86.62	27.62
5#	1.21	26.37	86.52	27.61
6#	1.20	26.52	86.23	27.44
7#	1.20	26.61	86.61	27.66
8#	1.20	26.54	86.59	27.58
9#	1.20	26.59	86.62	27.64
10#	1.21	26.47	86.18	27.60
11#	1.20	26.58	86.60	27.62
12#	1.21	26.47	86.59	27.73
13#	1.20	26.55	86.57	27.58
14#	1.21	26.54	86.58	27.80
15#	1.21	26.35	86.59	27.61
16#	1.20	26.56	86.60	27.60
17#	1.21	26.37	86.51	27.60
18#	1.20	26.63	86.57	27.66
19#	1.20	26.63	86.58	27.67
20#	1.21	26.43	86.29	27.60
	1.20±0.01	26.52±0.10	86.5±0.15	27.62±0.07

Supplementary Table 15 Certified PCE values of recently reported high-performance rigid and flexible pero-SCs.

Device types	year	PCE (%)	V_{oc} (V)	J_{sc} (mA/cm^2)	FF (%)	Ref.
rigid	2026	27.69	1.20	26.59	86.64	This work
	2024	25.74	1.188	25.73	84.17	*Nature*, **2024**, 632, 301-306
	2024	26.54	1.192	26.47	84.11	*Nature*, **2024**, 632, 536-542
	2025	26.08	1.185	26.27	83.84	*Nat. Energy*, **2025**, 10, 342-353
	2025	26.3	1.19	25.8	85.7	*Science*, **2025**, 389, 195
	2025	26.39	1.185	26.15	85.11	*Nat. Commun.*, **2025**, 16, 86
	2025	26.6	1.190	26.2	85.3	*Nat. Mater.*, **2025**, 24, 1265-1272
	2025	26.72	1.197	26.21	85.17	*Nat. Photon.*, **2025**, 19, 1070-1077
	2025	26.81	1.186	26.17	86.37	*Energy Environ. Sci.*, **2025**,18, 3196-3210
	2025	26.92	1.185	26.18	86.75	*Nature*, **2025**, 646, 95-101
	2025	27.15	1.192	26.71	85.31	*Science*, **2025**, 390, 638-642
	2026	27.57%	1.208	26.62	85.75	*Science*, **2025**, 392, 742-748
flexible	2026	26.64	1.21	26.27	84.36	This work
	2024	24.04	1.171	24.56	83.56	*Joule*, **2024** 8, 1120
	2024	24.41	1.183	25.66	80.38	*Energy Environ. Sci.*, **2024**, 17, 8162
	2024	24.48	1.152	25.51	83.31	*Adv. Mater.*, **2024**, 36, 2403531
	2024	24.9	1.188	25.29	83.5	*iEnergy*, **2024**, 3, 39
	2025	25.44	1.186	26.03	82.4	*Adv. Funct. Mater.*, **2025**, 35, 2424191
	2025	26.22	1.196	26.02	84.3	*Nat. Synth.*, **2025**, 5, 209-220

Supplementary Table 16 Statistical of the UV irradiation stability in references.

References	Initial PCE	Power (mW cm^{-2})	Time (h)	PCE decay
This work	26.84%	56.0	1080	81%
Nature, **2023**, 623, 313	25.5%	0.1	1100	95%
Sci. Adv., **2025**, 11, eadu3493	26.0%	17.0	500	80%
Joule, **2024**, 8, 11, 3142	26.32%	--	110	90%
Adv. Energy Mater., **2025**, 15, 2501296	24.68%	50	130	80%
Adv. Funct. Mater., **2024**, 34, 2400474	24.73%	50	380	90%
Chem. Eng. J., **2024**, 497, 154552	22.46%	50	250	91%

Supplementary Table 17 The initial photovoltaic parameters of pero-SCs under different stability protocols (under AM 1.5G illumination, the light emitting diode (LED), light emitting plasma (LEP), metal halide lamp (MH) solar simulator, 100 mW cm^{-2}).

protocols	SAMs	V_{oc} (V)	J_{sc} (mA/cm^2)	FF (%)	PCE (%)
ISOS-D-2	2PACz	1.16±0.01	26.45±0.08	80.4±0.7	24.66±0.25
	FTPA-CPA	1.18±0.01	26.57±0.13	82.1±0.3	25.70±0.18
	FMTPA-CPA	1.20±0.01	26.59±0.05	83.5±0.3	26.68±0.19
ISOS-T-3	2PACz	1.16±0.01	26.45±0.08	80.5±0.7	24.70±0.26
	FTPA-CPA	1.19±0.01	26.47±0.08	82.1±0.5	25.74±0.22
	FMTPA-CPA	1.20±0.01	26.59±0.07	83.4±0.3	26.69±0.20
ISOS-L-2	2PACz	1.16±0.01	25.81±0.12	80.8±0.5	24.19±0.28
	FTPA-CPA	1.19±0.01	25.89±0.07	82.8±0.4	25.44±0.17
	FMTPA-CPA	1.20±0.01	25.99±0.08	83.9±0.4	26.25±0.13
ISOS-LC-1	2PACz	1.16±0.01	25.69±0.10	80.6±0.5	24.11±0.25
	FTPA-CPA	1.19±0.01	25.78±0.08	82.3±0.5	25.17±0.15
	FMTPA-CPA	1.21±0.01	25.90±0.04	83.3±0.7	26.00±0.11
ISOS-D-3	2PACz	1.16±0.01	26.39±0.12	80.3±0.5	24.59±0.22
	FTPA-CPA	1.18±0.01	26.45±0.10	82.3±0.6	25.77±0.11
	FMTPA-CPA	1.20±0.01	26.56±0.06	83.8±0.8	26.74±0.15
UV irradiation	2PACz	1.17±0.01	26.46±0.09	80.5±0.4	24.89±0.25
	FTPA-CPA	1.19±0.01	26.51±0.08	81.8±0.6	25.82±0.08
	FMTPA-CPA	1.20±0.01	26.58±0.05	83.9±0.6	26.84±0.10
MPPT (MH lamp)	2PACz	1.17±0.01	25.55±0.09	80.2±0.7	23.91±0.29
	FTPA-CPA	1.19±0.01	25.58±0.07	82.1±0.7	25.01±0.17
	FMTPA-CPA	1.21±0.01	25.69±0.03	84.0±0.8	26.02±0.13
MPPT at 85±5℃ (LEP lamp)	2PACz	1.17±0.01	25.90±0.14	80.8±0.7	24.46±0.31
	FTPA-CPA	1.19±0.01	26.01±0.07	81.5±0.9	25.25±0.20
	FMTPA-CPA	1.21±0.01	26.06±0.06	83.7±0.8	26.30±0.12
MPPT at 85±5℃ (MH lamp)	2PACz	1.17±0.01	25.69±0.07	80.9±0.9	24.26±0.28
	FTPA-CPA	1.19±0.01	25.73±0.06	81.9±0.6	25.04±0.16
	FMTPA-CPA	1.21±0.01	25.78±0.05	83.6±0.8	26.01±0.10

The average PCE, and standard deviations of 10 devices.

Supplementary Table 18 XPS spectra analysis obtained from the 2PACz, FTPA-CPA and FMTPA-CPA films under multiple failure mechanism.

SAMs	aging condition	In area	P area	P/In
Pristine 2PACz	high temperature (85±5℃ for 1000 h)	934131.1	6941.9	0.0074
	light illumination (1000 h)	1013991.6	7161.9	0.0071
	electrical bias stressing (-2.0 V for 10 h)	456323.6	3250.8	0.0071
	high humidity (85±5% RH for 1000 h)	449742.3	3328.3	0.0074
	bending stress (10000 cycles, 5 mm radius)	1189163.5	8670.6	0.0073
2PACz high temperature (85±5℃ for 1000 h)	pristine	934131.1	6941.9	0.0074
	with PbI_2	956322.7	6747.3	0.0071
	with FAI	1212534.1	6328.3	0.0052
	with AcOH	753585.3	2284.5	0.0030
FTPA-CPA high temperature (85±5℃ for 1000 h)	pristine	524176.6	7426.3	0.0142
	with PbI_2	422221.2	6092.6	0.0144
	with FAI	464195.2	4592.3	0.0099
	with AcOH	654074.1	5560.1	0.0085
FMTPA-CPA high temperature (85±5℃ for 1000 h)	pristine	193731.8	4428.4	0.0229
	with PbI_2	289357.9	6713.9	0.0232
	with FAI	325733.1	7495.7	0.0230
	with AcOH	198972.6	4582.4	0.0230

Supplementary Table 19 Photovoltaic parameters of pero-SCs based on FMTPA-CPA using different processing solvents under AM1.5G, 100 mW/cm^2 illumination. Forward scan: –0.2 V→1.2 V; Reverse scan: 1.2 V→ –0.2 V.

Processing solvent	V_{oc} (V)	J_{sc} (mA/cm^2)	FF (%)	PCE_{max}[a](PCE_{avg})[a] (%)
IPA	1.21	26.63	84.53	27.24 (27.03±0.10)
EtOH	1.21	26.43	84.47	27.01 (26.79±0.12)
CB	1.21	26.69	84.38	27.25 (27.04±0.09)
TOL	1.21	26.49	83.99	26.92 (26.73±0.09)

[a] The maximum PCE, average PCE, and standard deviations of 20 devices.

Supplementary Table 20 Photovoltaic parameters of pero-SCs based on a wide-bandgap (1.83 eV) triple cation perovskite under AM1.5G, 100 mW/cm^2 illumination. Forward scan: –0.2 V→1.35 V; Reverse scan: 1.35 V→ –0.2 V.

SAMs	Scan direction	V_{oc} (V)	J_{sc} (mA/cm^2)	FF (%)	PCE (%)
FMTPA-CPA	Reverse	1.33	16.81	84.05	18.79
	Forward	1.32	16.80	83.26	18.46

References

1 Grimme, S., Ehrlich, S. & Goerigk, L. Effect of the damping function in dispersion corrected density functional theory. *J. Comput. Chem.* **32**, 1456-1465 (2011).

2 Tang, H. *et al.* A solution-processed n-type conducting polymer with ultrahigh conductivity. *Nature* **611**, 271-277 (2022).

3 Jiang, Y. *et al.* Suppressing electron-phonon coupling in organic photovoltaics for high-efficiency power conversion. *Nat. Commun.* **14**, 5079 (2023).

4 Zheng, D. & Wang, F. Performing Molecular Dynamics Simulations and Computing Hydration Free Energies on the B3LYP-D3(BJ) Potential Energy Surface with Adaptive Force Matching: A Benchmark Study with Seven Alcohols and One Amine. *ACS Physical Chemistry Au* **1**, 14-24 (2021).

5 Taniguchi, T. Analysis of Molecular Configuration and Conformation by (Electronic and) Vibrational Circular Dichroism: Theoretical Calculation and Exciton Chirality Method. *Bulletin of the Chemical Society of Japan* **90**, 1005-1016 (2017).

6 Seco, J. M., Quiñoá, E. & Riguera, R. The Assignment of Absolute Configuration by NMR. *Chem. Rev.* **104**, 17-118 (2004).

7 Babinský, M., Bouzková, K., Pipíška, M., Novosadová, L. & Marek, R. Interpretation of Crystal Effects on NMR Chemical Shift Tensors: Electron and Shielding Deformation Densities. *The Journal of Physical Chemistry A* **117**, 497-503 (2013).

8 Anson, C. W. & Thamattoor, D. M. Influence of Substituents on the Through-Space Shielding of Aromatic Rings. *The Journal of Organic Chemistry* **77**, 1693-1700 (2012).

9 Li, Y. *et al.* Merocyanine with Hole-Transporting Ability and Efficient Defect Passivation Effect for Perovskite Solar Cells. *ACS Energy Lett.* **6**, 869-876 (2021).

10 Qu, G. *et al.* Self-assembled materials with an ordered hydrophilic bilayer for high performance inverted Perovskite solar cells. *Nat. Commun.* **16**, 86 (2025).

11 Luo, Y. *et al.* Bulk nano-heterointerface secures molecular contacts in perovskite solar cells. *Nat. Mater.* (2026), https://doi.org/10.1038/s41563-026-02546-1.

12 Xie, Y. *et al.* Thiophene Expanded Self-Assembled Monolayer as Hole Transport Layer for Organic Solar Cells with Efficiency of 20.78%. *Adv. Mater.* **37**, e02485 (2025).

13 Wahab, A. & Gershoni-Poranne, R. Accelerated diradical character assessment in large datasets of polybenzenoid hydrocarbons using xTB fractional occupation. *Physical Chemistry Chemical Physics* **27**, 5973-5983 (2025).

14 Neese, F., Wennmohs, F., Becker, U. & Riplinger, C. The ORCA quantum chemistry program package. *J. Chem. Phys* **152**, 224108 (2020).

15 Gaussian 16, Revision B.01 (Gaussian, Inc., Wallingford CT, 2016).

16 Lu, T. A comprehensive electron wavefunction analysis toolbox for chemists, Multiwfn. *J. Chem. Phys* **161**, 082503 (2024).

17 Lu, T. & Chen, F. Multiwfn: A multifunctional wavefunction analyzer. *J. Comput. Chem.* **33**, 580-592 (2012).
18 Pliego, J. R. Thermodynamic cycles and the calculation of pKa. *Chemical Physics Letters* **367**, 145-149 (2003).
19 Kresse, G. & Furthmüller, J. Efficient iterative schemes for ab initio total-energy calculations using a plane-wave basis set. *Physical Review B* **54**, 11169-11186 (1996).
20 Kresse, G. & Hafner, J. Ab initio molecular dynamics for open-shell transition metals. *Physical Review B* **48**, 13115-13118 (1993).
21 Abraham, M. J. *et al.* GROMACS: High performance molecular simulations through multi-level parallelism from laptops to supercomputers. *SoftwareX* **1-2**, 19-25 (2015).
22 Wang, J., Wolf, R. M., Caldwell, J. W., Kollman, P. A. & Case, D. A. Development and testing of a general amber force field. *J. Comput. Chem.* **25**, 1157-1174 (2004).
23 Hess, B., Bekker, H., Berendsen, H. J. C. & Fraaije, J. G. E. M. LINCS: A linear constraint solver for molecular simulations. *J. Comput. Chem.* **18**, 1463-1472 (1997).
24 Parrinello, M. & Rahman, A. Polymorphic transitions in single crystals: A new molecular dynamics method. *Journal of Applied Physics* **52**, 7182-7190 (1981).
25 Bussi, G., Donadio, D. & Parrinello, M. Canonical sampling through velocity rescaling. *J. Chem. Phys* **126**, 014101 (2007).
26 Essmann, U. *et al.* A smooth particle mesh Ewald method. *J. Chem. Phys* **103**, 8577-8593 (1995).
27 Humphrey, W., Dalke, A. & Schulten, K. VMD: Visual molecular dynamics. *Journal of Molecular Graphics* **14**, 33-38 (1996).
28 Kohn, W. & Sham, L. J. Self-Consistent Equations Including Exchange and Correlation Effects. *Physical Review* **140**, A1133-A1138 (1965).
29 Kresse, G. & Furthmüller, J. Efficiency of ab-initio total energy calculations for metals and semiconductors using a plane-wave basis set. *Computational Materials Science* **6**, 15-50 (1996).
30 Kresse, G. & Joubert, D. From ultrasoft pseudopotentials to the projector augmented-wave method. *Physical Review B* **59**, 1758-1775 (1999).
31 Blöchl, P. E. Projector augmented-wave method. *Physical Review B* **50**, 17953-17979 (1994).
32 Coropceanu, V. *et al.* Charge Transport in Organic Semiconductors. *Chem. Rev.* **107**, 926-952 (2007).
33 Fei, C. *et al.* Limiting phosphonic acid interlayer–perovskite reactivity to stabilize perovskite solar modules. *Science* **391**, 6780-6788 (2026).
34 Ahn, N. *et al.* Trapped charge-driven degradation of perovskite solar cells. *Nat. Commun.* **7**, 13422 (2016).
35 Dunfield, S. P. *et al.* From Defects to Degradation: A Mechanistic Understanding of Degradation in Perovskite Solar Cell Devices and Modules. *Adv. Energy Mater.* **10**, 1904054 (2020).

36 Marcus, Y. The properties of organic liquids that are relevant to their use as solvating solvents. *Chemical Society Reviews* **22**, 409-416 (1993).
37 Bythell, B. J., Suhai, S., Somogyi, Á. & Paizs, B. Proton-Driven Amide Bond-Cleavage Pathways of Gas-Phase Peptide Ions Lacking Mobile Protons. *JACS* **131**, 14057-14065 (2009).
38 Pol, M. D. *et al.* Guiding Transient Peptide Assemblies with Structural Elements Embedded in Abiotic Phosphate Fuels. *Angew. Chem. Int. Ed* **63**, e202404360 (2024).
39 Fei, C. *et al.* Strong-bonding hole-transport layers reduce ultraviolet degradation of perovskite solar cells. *Science* **384**, 1126-1134 (2024).